Article

Developmental Cell

Accumulation of APP C-terminal fragments causes endolysosomal dysfunction through the dysregulation of late endosome to lysosome-ER contact sites

Graphical abstract

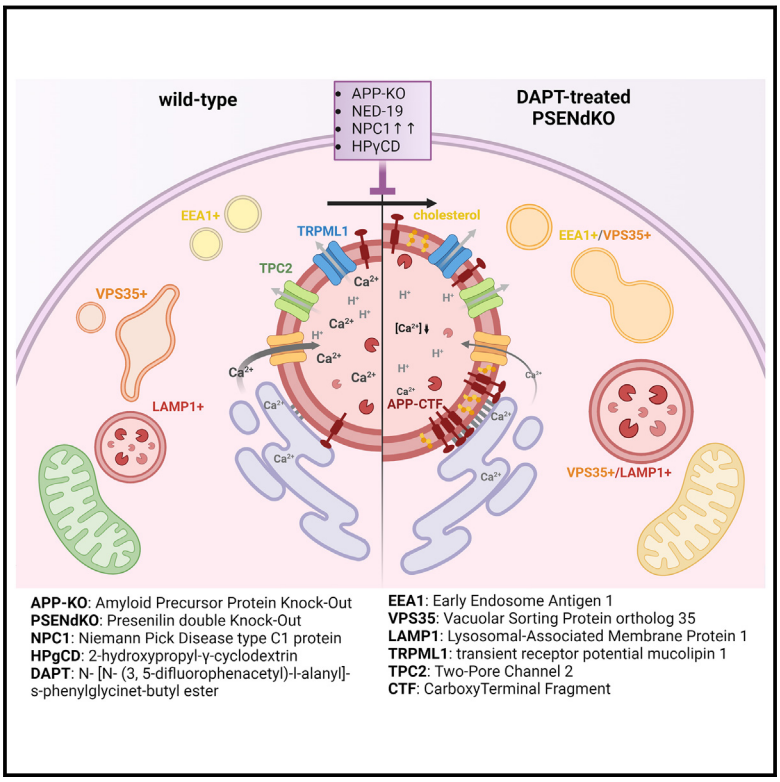

Highlights

- Decreased lysosomal Ca^{2+} is an initial event following chronic γ-secretase inhibition
- Lysosomal Ca^{2+} deficits correlate with APP-CTF accretion in or near LE/Lys-ER contacts
- Balanced APP-CTF levels are required for lysosomal homeostasis
- γ-Secretase activity is needed to abrogate APP function, as opposed to Notch signaling

Authors

Marine Bretou, Ragna Sannerud, Abril Escamilla-Ayala, ..., Keimpe Wierda, Eeva-Liisa Eskelinen, Wim Annaert

Correspondence

wim.annaert@kuleuven.be

In brief

Neuronal endosomal and lysosomal abnormalities are early signs of Alzheimer's disease. Bretou et al. identified lysosomal calcium deficits triggered by γ-secretase inhibition. This initiated a cascade leading to endolysosomal demise, originating from impaired APP proteolysis disrupting inter-organellar communication between lysosomes and the endoplasmic reticulum.

Bretou et al., 2024, Developmental Cell *59*, 1–22
June 17, 2024
https://doi.org/10.1016/j.devcel.2024.03.030

CellPress

Developmental Cell

CellPress
OPEN ACCESS

Article

Accumulation of APP C-terminal fragments causes endolysosomal dysfunction through the dysregulation of late endosome to lysosome-ER contact sites

Marine Bretou,[1,2] Ragna Sannerud,[1,2] Abril Escamilla-Ayala,[3] Tom Leroy,[1,2] Céline Vrancx,[1,2] Zoë P. Van Acker,[1,2] Anika Perdok,[1,2] Wendy Vermeire,[1,2] Inge Vorsters,[1,2] Sophie Van Keymolen,[1,2] Michelle Maxson,[4] Benjamin Pavie,[3] Keimpe Wierda,[5] Eeva-Liisa Eskelinen,[6] and Wim Annaert[1,2,7,*]

[1]Laboratory for Membrane Trafficking, VIB-Center for Brain and Disease Research, Leuven, Belgium
[2]Department of Neurosciences, KU Leuven, Leuven, Belgium
[3]VIB-BioImaging Core, VIB-Center for Brain and Disease Research, Leuven, Belgium
[4]Cell Biology Program, The Hospital for Sick Children, Department of Biochemistry, University of Toronto, Toronto, Canada
[5]Electrophysiology Expertise Unit, VIB-Center for Brain and Disease Research, Leuven, Belgium
[6]Institute of Biomedicine, University of Turku, Turku, Finland
[7]Lead contact
*Correspondence: wim.annaert@kuleuven.be
https://doi.org/10.1016/j.devcel.2024.03.030

SUMMARY

Neuronal endosomal and lysosomal abnormalities are among the early changes observed in Alzheimer's disease (AD) before plaques appear. However, it is unclear whether distinct endolysosomal defects are temporally organized and how altered γ-secretase function or amyloid precursor protein (APP) metabolism contribute to these changes. Inhibiting γ-secretase chronically, in mouse embryonic fibroblast and hippocampal neurons, led to a gradual endolysosomal collapse initiated by decreased lysosomal calcium and increased cholesterol, causing downstream defects in endosomal recycling and maturation. This endolysosomal demise is γ-secretase dependent, requires membrane-tethered APP cytoplasmic domains, and is rescued by APP depletion. APP C-terminal fragments (CTFs) localized to late endosome/lysosome-endoplasmic reticulum contacts; an excess of APP-CTFs herein reduced lysosomal Ca^{2+} refilling from the endoplasmic reticulum, promoting cholesterol accretion. Tonic regulation by APP-CTFs provides a mechanistic explanation for their cellular toxicity: failure to timely degrade APP-CTFs sustains downstream signaling, instigating lysosomal dyshomeostasis, as observed in prodromal AD. This is the opposite of substrates such as Notch, which require intramembrane proteolysis to initiate signaling.

INTRODUCTION

Presenilin 1 and 2 (PSEN1 and 2) are the catalytic subunits of γ-secretase that proteolyze the amyloid precursor protein (APP), resulting in amyloid β peptides (Aβs) of various lengths.[1,2] Dominantly inherited mutations in the *APP* and *PSEN* genes, linked to familial Alzheimer's disease (FAD), decrease γ-secretase processivity,[3] shifting production to longer, more aggregation-prone Aβ peptides and accelerating Aβ deposition in senile plaques in AD patients' brains.[4] However, there is ongoing debate about the extent of toxic Aβs' role in triggering and/or driving the neurodegenerative cascade in Alzheimer's disease (AD).[5,6]

Importantly, autolysosomal dysfunction is implicated in AD etiopathology, as observed in post-mortem AD brains.[7] In the AD brain[8] and murine models,[9,10] abnormally enlarged endosomes precede the appearance of extracellular amyloid plaques and neurofibrillary tangles, making them early pathobiological signs of neuronal demise.[1] Genetic evidence supports the importance of an altered endolysosomal homeostasis,[11] as genome-wide association studies have identified late-onset AD-associated risk variants in genes linked to cholesterol metabolism, endocytic transport regulation, and lysosomal processes.[12–14] Endolysosomal pathology is a convergent mechanism shared with monogenic FAD.[8,15–18]

Kwart et al. found enlarged Rab5-positive endosomes in induced pluripotent stem cell (iPSC)-derived human neurons with FAD APP or PSEN1 mutations, which worsened with combined mutations, suggesting a synergistic effect on the endolysosome system.[17] Hung and co-workers observed common defects in lysosomal and autophagic pathways due to APP and PSEN1 mutations.[18] Additionally, APP-mediated enlargement of Rab5-positive endosomes disrupted axonal trafficking[19] and nerve growth factor signals,[20] leading to cell death. Herein, APPL1 recruitment may contribute to endosomal abnormalities by stabilizing Rab5-GTP,[19] associating Rab5 overactivation

Please cite this article in press as: Bretou et al., Accumulation of APP C-terminal fragments causes endolysosomal dysfunction through the dysregulation of late endosome to lysosome-ER contact sites, Developmental Cell (2024), https://doi.org/10.1016/j.devcel.2024.03.030

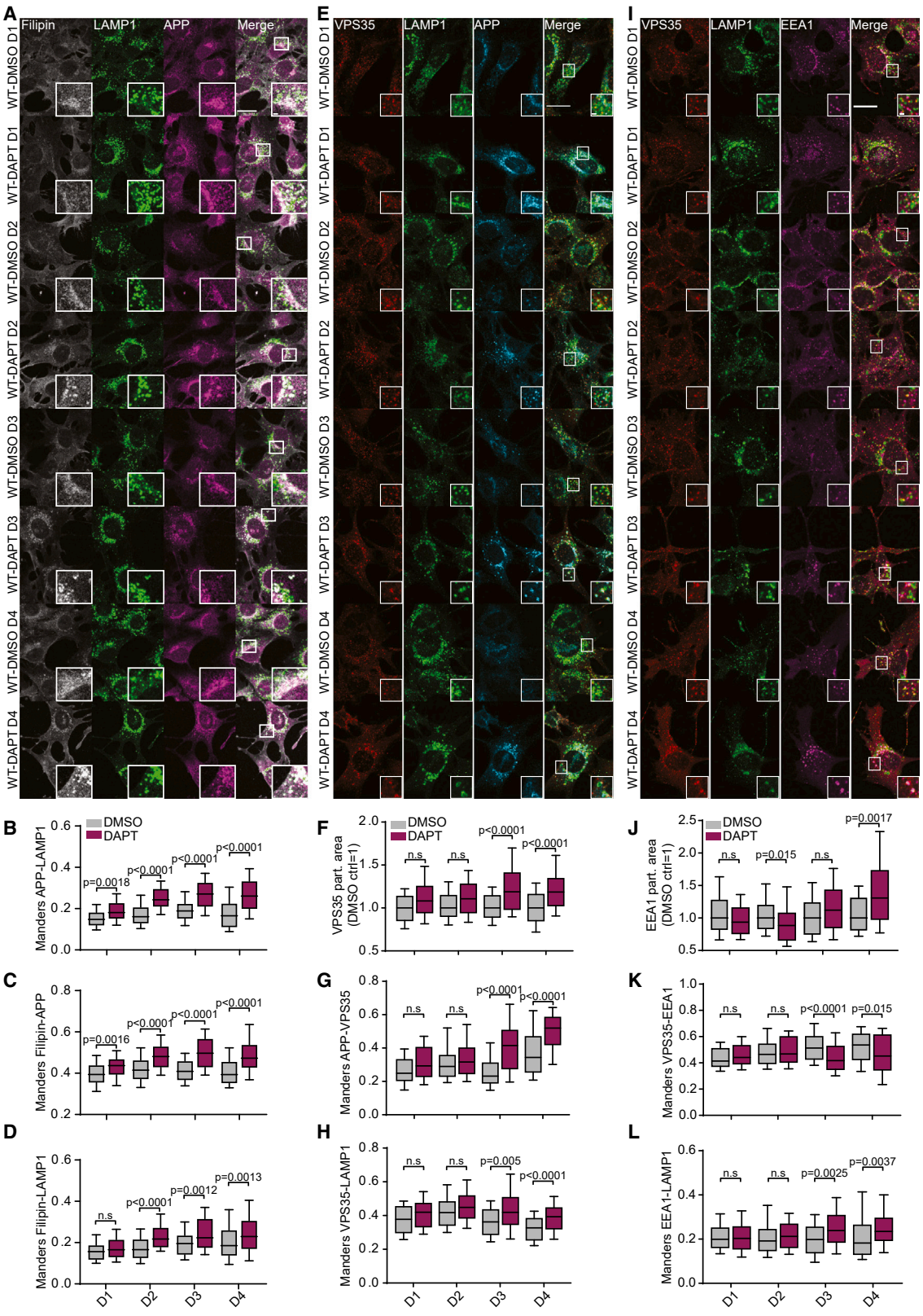

(legend on next page)

Please cite this article in press as: Bretou et al., Accumulation of APP C-terminal fragments causes endolysosomal dysfunction through the dysregulation of late endosome to lysosome-ER contact sites, Developmental Cell (2024), https://doi.org/10.1016/j.devcel.2024.03.030

early in the cascade leading to endolysosomal dyshomeostasis. The roles of APP and PSEN1 require further clarification, but perturbation of endocytic compartments could alter APP proteolytic fragment abundance and quality. Conversely, FAD-linked mutations in APP and PSENs may disrupt endosolysosomal homeostasis and degradative capacity. Although intracellular Aβ42 toxicity has been linked to late endosomes, attention now focuses on APP β C-terminal fragments (βCTFs) in endolysosomal dysfunction.[16–18,21] In support of this notion, BACE-1 inhibition corrected endosomal,[17] lysosomal, and autophagic[18] defects in models with FAD-linked PSEN1 or APP and SorL1 variants.[21] Depleting APP also mitigated late defects in lysosomal or autophagic pathways.[18]

If these recent reports highlighted the role of APP-CTFs, PSENs on their own also regulate endolysosomal homeostasis through various mechanisms. PSEN deficiency or PSEN1 FAD mutations may impair lysosomal acidification via a failing V-ATPase,[22,23] while other studies emphasized dysregulation in lysosomal Ca^{2+} homeostasis[24,25] and nutrient sensing and CLEARance.[26,27] Notably, defects are evident throughout the endolysosomal pathway, up to affecting autophagy, but their chronological initiation is unclear. For instance, excess APP-β-CTFs may induce early endosomal disturbances, yet their precise mechanism is uncertain.[17] But, conversely, APP-βCTFs appeared recently to tonically regulate V-ATPase, arguing for a primary defect in later compartments, including lysosomes.[28]

To address these questions, we used CRISPR-Cas9 editing to generate novel combined PSEN double knockout (PSENdKO) and APP KO cells that allowed us to systematically dissect the contribution of these genes in otherwise isogenic backgrounds. We conclusively show that a build-up of APP-CTFs caused by PSEN/γ-secretase inactivation abruptly affects lysosomal Ca^{2+} homeostasis, resulting in a cascade of events disturbing endosomal recycling and sorting compartments and, consequently, provoking a collapse in endolysosomal maturation. APP KO rescued these chronological defects, which can be mimicked by re-introducing a membrane-tethered APP intracellular domain (AICD), narrowing down the effect to downstream APP-CTFs signaling. Mechanistically, we explain this by the accretion of APP-CTFs at or near late endosome/lysosome (LE/Lys)-endoplasmic reticulum (ER) contact sites, affecting lysosomal Ca^{2+} refilling from the ER. Our findings imply a critical role for balanced APP-CTF levels in LE/Lys-ER membrane contact sites (MCSs) to maintain endolysosomal homeostasis. The detrimental effects of elevated APP-CTFs herein underscore their significance as a therapeutic target to address AD progression at an early stage, preceding the appearance of amyloid plaques.

RESULTS

Inhibition of γ-secretase induces lysosomal dysfunction prior to affecting endosomes

To address the sequence of events leading to the observed broad failure of the endolysosomal system, we treated wild-type (WT) mouse embryonic fibroblasts (MEFs) with the γ-secretase inhibitor, N-[N-(3,5-difluorophenacetyl)-l-alanyl]-s-phenylglycinet-butyl ester (DAPT), for 4 days (1 μM). DAPT-treated cells rapidly accumulated APP-CTFs (Figure S1A) in lysosomal-associated membrane protein 1 (LAMP1)-positive LE/Lys (Figures 1A and 1B). This accumulation strongly correlated with a significantly reduced lysosomal Ca^{2+} content, evaluated in Fura2-AM-loaded cells challenged with Gly-Phe-b-naphtylamide (GPN)[29–31] (Figure S1B). In addition, DAPT-treated cells started to accumulate cholesterol in LE/Lys; however, only significantly from day 2 (Figures 1A–1D). When investigating endosomal compartments, vacuolar protein sorting ortholog 35 (VPS35)-positive organelle size was increased (Figures 1E and 1F), underscoring a potential defect in endosomal recycling, although this only took place following 3 days of DAPT treatment and thus downstream of lysosomal dysfunctions. Importantly, early endosomes, as identified through early endosome antigen-1 (EEA1), became significantly enlarged only after 4 days of treatment, indicating a late event (Figures 1I and 1J). Increased organelle size coincided with increased co-localization of VPS35 and EEA1 with LAMP1, suggesting a general delay in endosome-to-lysosome maturation and a progressive partial collapse of early and late endosomal compartments in DAPT-treated cells (Figures 1H–1L). This is further corroborated by increased co-localization of APP-CTFs in collapsing early to late and recycling endosomes (Figures 1B and 1G). Notably, similar results were obtained in primary mouse hippocampal neurons, already showing a significantly decreased lysosomal Ca^{2+} response after 1 day of DAPT treatment (Figure S1C), whereas an increased co-localization of EEA1- and VPS35-positive endosomes with LAMP1-positive lysosomes was only evident following 4 days of treatment (Figures 2A–2D and S1D). The overall endolysosomal collapse was further substantiated by an increased particle area of endolysosomal compartments and accretion of APP-CTFs in VPS35 and LAMP1-positive compartments (Figures 2E–2J and S1E). These data support a conserved chronology in which lysosomal dysfunction lies at

Figure 1. Chronic γ-secretase inhibition identifies a chronology in endolysosomal defects

(A) Immunostaining for APP (magenta) and LAMP1 (green) versus filipin (gray) in MEFs treated with DAPT (1 μM) or DMSO for 1–4 days.

(B–D) Mander's overlap coefficient (MOC) for APP-LAMP1 (B), filipin-APP (C), and filipin-LAMP1 (D). APP-CTFs accumulated from day 1, while cholesterol only from day 2 onward ($N = 2$, with, from left to right, $n = 112, 109, 120, 111, 127, 123, 120$, and 127 cells).

(E) Immunostaining for VPS35 (red), LAMP1 (green), and APP (cyan).

(F) Size of $VPS35^+$ compartments ($N \geq 2$, with $n = 60, 63, 70, 62, 68, 65, 84$, and 83 cells, normalized to DMSO).

(G and H) MOC for APP-VPS35 (G) and VPS35-LAMP1 (H). $VPS35^+$ compartments significantly enlarged from day 3 ($N \geq 2$, with $n = 60, 63, 70, 62, 68, 65, 84$, and 83 cells).

(I) Immunostaining for VPS35 (red), LAMP1 (green), and EEA1 (magenta).

(J) $EEA1^+$ compartments enlarged from day 4 ($N = 2$, with $n = 113, 114, 96, 103, 72, 93, 77$, and 66 cells, normalized to DMSO).

(K and L) MOC for VPS35-EEA1 (K) and EEA1-LAMP1 (L). Endolysosomal collapse is detected from day 3 ($N = 2$, with $n = 97, 114, 96, 103, 73, 93, 77$, and 66 cells, normalized to DMSO). For all box-and-whiskers graphs: boxes display the 25/75, and whiskers the 10/90 percentiles. Multiple ANOVA Kruskal-Wallis with Dunn's post hoc test were applied. Scale bars, 20 μm; inset 2 μm.

Please cite this article in press as: Bretou et al., Accumulation of APP C-terminal fragments causes endolysosomal dysfunction through the dysregulation of late endosome to lysosome-ER contact sites, Developmental Cell (2024), https://doi.org/10.1016/j.devcel.2024.03.030

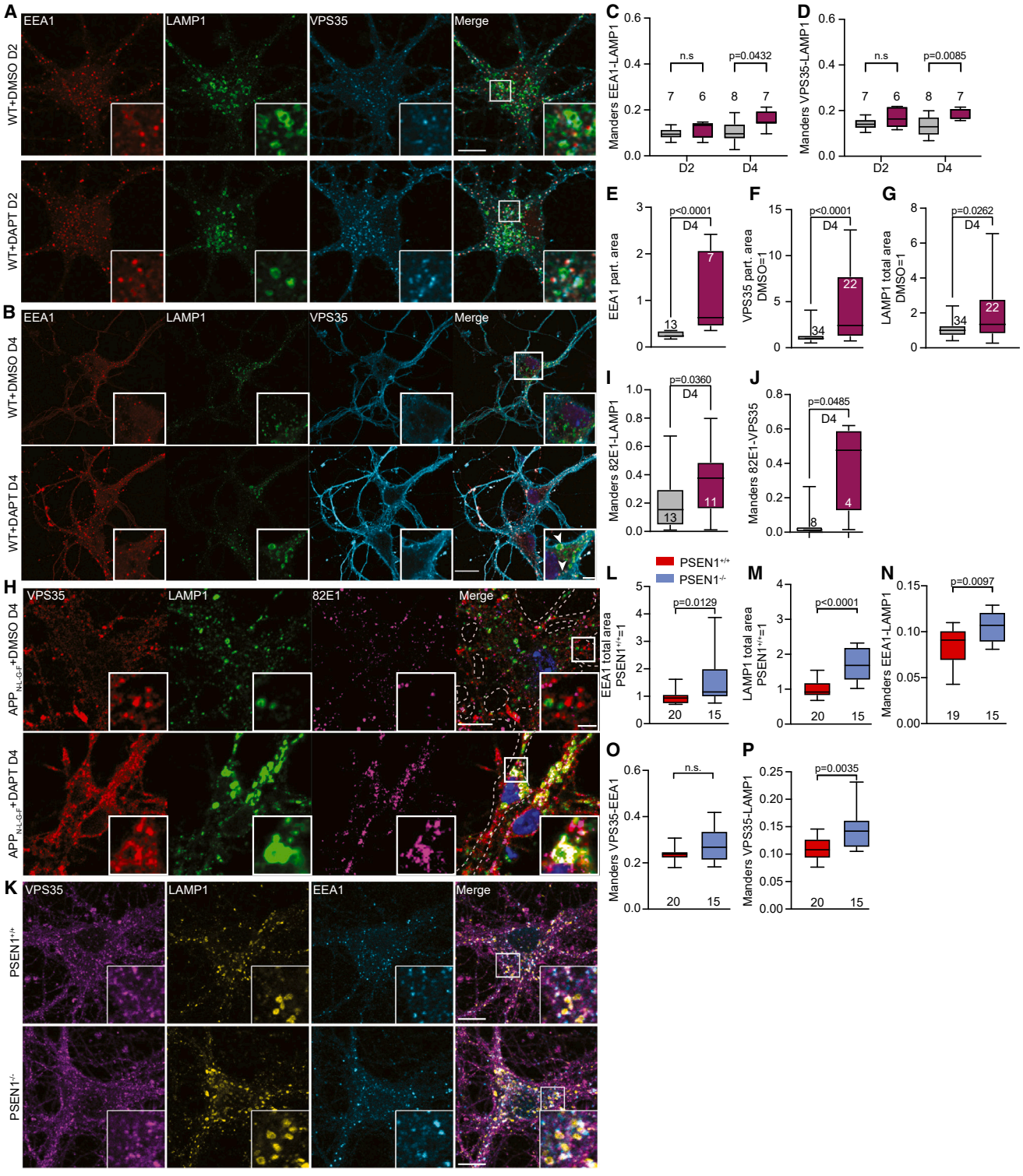

Figure 2. Chronic γ-secretase inhibition or PSEN depletion impact on neuronal endosomes and lysosomes

(A and B) Immunostaining for EEA1 (red), LAMP1 (green), and VPS35 (cyan), in PSEN1$^{+/+}$ primary hippocampal neurons treated with DMSO or DAPT for 2 (A) or 4 (B) days (scale bars: 10 μm in A and 20 μm in B; inset 5 μm).

(C and D) Significant increased co-localization of EEA1-LAMP1 (C) and VPS35-LAMP1 (D) at day 4, suggesting delayed endolysosomal maturation.

(E–J) Size of EEA1 (E), VPS35 (F), and LAMP1 (G) compartments following 4 days DAPT (*N* = 1 in E, or *N* = 3 in F and G, normalized to DMSO). (H) Immunostaining for VPS35 (red), LAMP1 (green), and 82E1 (magenta) in APP-NLGF neurons (DIV14), with DMSO or DAPT (4 days; scale bars, 10 μm; inset 2 μm).

(legend continued on next page)

the root of the endolysosomal collapse. DIV 14 primary hippocampal neurons deficient for PSEN1 chiefly recapitulated endosomal and lysosomal enlargements, decreased lysosomal Ca^{2+}, and endolysosomal collapse, as evidenced from the increased co-localization of EEA1 and VPS35 with LAMP1 (Figures 2K–2P and S1F). Interestingly, we found VPS35 to be co-localized with ICAM5 (Figure S1G), a neuronal adhesion molecule previously found to aberrantly accumulate in autophagic-like vacuoles in PSEN1$^{-/-}$ hippocampal neurons,[32,33] suggesting that the endolysosomal collapse may route dysfunctional organelles ultimately to autophagy.

Knocking out APP in PSENdKO cells corrects endolysosomal dysfunctions

Given the direct link between APP processing and endolysosomal defects, observed here and by others,[17,18] we decided to decipher the underlying mechanistic role of, in particular, APP-CTFs. Given the similar negative effects of chronic γ-secretase inhibition on endolysosomal maturation between non-neuronal cells and primary neurons, we chose to use PSEN-deficient MEFs in the next experiments. Independent PSENdKO MEF clones[2] were stably rescued with human PSEN1 (hPSEN1) using retroviral transduction. Nicastrin (NCT) maturation was restored as well as PEN2 stabilization, PSEN1 endoproteolysis, and APP-CTF clearance, indicating that PSEN1/γ-secretase expression and activity were rescued to WT levels (Figure S2A). As for DAPT-treated cells (Figures 1 and 2), deficiency of PSEN expression, and thus γ-secretase complex formation, resulted in a significantly reduced lysosomal Ca^{2+} content (Figure 3A). Only a concomitant minor alkalinization was observed, in agreement with previous reports by us and others (Figure S2B).[24–26] However, such a change is within the physiological variation of pH in lysosomes, i.e., between 4.5 and 5.0.[34] Moreover, only full alkalinization, by treating cells with bafilomycin1 (Baf1), resulted in an equally affected lysosomal Ca^{2+} content as observed in PSENdKO cells. Independent assessment of lysosomal pH using FIRE-phLy[35] did not show any significant difference between WT, PSENdKO, and hPSEN1-rescued MEFs (Figures S2C and S2D). As pH alteration in PSENdKO was suggested to be induced by an alteration of maturation and transport of the V-ATPase,[22] we detected no defects in the N-glycosylation of the endogenous V0a1 subunit of the V-ATPase nor in V-ATPase subunit levels in isolated lysosomes from WT, PSENdKO, and hPSEN1-rescued MEFs. Also, the ratio of V0 over V1 subunits was not affected, indicating normally assembled V-ATPases on lysosomes (Figures S2E–S2G). In further support, we next used Alexa568-conjugated SidK, a recombinant fragment of an effector protein from *Legionella pneumophila* that directly binds active V-ATPases.[36] SidK-Alexa568 displayed an increased co-localization with LAMP1 in PSENdKO compared with WT and hPSEN1-rescued PSENdKO MEFs, underscoring a higher, and not lower, abundancy of active V-ATPases on lysosomes (Figures S2H and S2I). Although this could be explained by the overall delay in endosomal maturation and endolysosomal collapse, these data together, strongly argue in favor of lysosomal Ca^{2+} defects being a primary cause of lysosomal dysfunctions in PSENdKO cells.

We subsequently gene-edited both WT and PSENdKO MEFs to knock out APP, ensuring isogenic backgrounds (Figure S2J). Depleting APP was sufficient to fully rescue the lysosomal Ca^{2+} defect caused by PSEN deficiency in independent clones to the same extent as observed in hPSEN1-rescued cells (Figures 3A, 3B, and S2J). It also did not significantly affect pH (Figures S2C and S2D) but rescued the increased levels of active V-ATPases in LAMP1-positive lysosomes of PSENdKO MEFs (Figures S2H and S2I), lending further support to lysosomal Ca^{2+} deficit as a primary cause of lysosomal dysfunctions in PSEN-deficient cells. Conversely, in the absence of APP expression, treatment with DAPT (1 μM, 4 days) did not affect the GPN-elicited Ca^{2+} response (Figures 3C and S2K). This further supports the notion of APP playing a direct role in the control and maintenance of lysosomal Ca^{2+} homeostasis and, thus, being involved early in the endolysosomal collapse cascade.

PSENdKO cells displayed enlarged LAMP1- and EEA1-positive compartments as well as an increased recruitment of VPS35 to these organelles (Figures 3D–3H, 3J, and 3K). In agreement with our observations in DAPT-treated cells, the significantly increased co-localization of EEA1-LAMP1 (Figure 3I), VPS35-EEA1 (Figure 3J), and VPS35-LAMP1-positive structures (Figure 3K) supports a general delay/collapse in endosomal maturation. VPS35 levels were maintained between cell lines, excluding the enlargements to be grounded in an altered retromer expression (Figure S2L). Of note, both VPS35-positive and LAMP1-positive structures in PSENdKO cells accumulate APP, likely APP-CTFs, and this accumulation is relieved when hPSEN1 is re-introduced (Figures S2M–S2O). Re-expression of hPSEN1, as well as depletion of APP, reduced the size of EEA1-positive and VPS35-positive organelles and decreased the co-localization of endosomal markers, thus alleviating the delay in endolysosomal maturation (Figures 3D–3K). On the ultrastructural level, transmission electron microscopy (TEM) revealed enlarged multivesicular bodies (MVBs) with fewer intraluminal vesicles in PSENdKO as compared with hPSEN1 WT as well as APP-depleted cells (Figures 3L–3N, S3A, and S3B). This is consistent with a maturation delay and with immature MVBs accumulating at an early stage in the degradative pathway, i.e., at the crossroads of recycling and degradation.[37] Of note, APP depletion did not revert the increased lysosomal area back to WT, in agreement with APP being required for the proper maintenance of endolysosomal size.[38]

In addition to endolysosomal defects, the trafficking of raft-associated components such as GM1 gangliosides (evidenced by CtxB Alexa-488) and caveolin-1 (Cav1) was altered upon PSEN depletion. When cells were brought to suspension,

(I and J) MOC showing that DAPT treatment (4 days) caused βCTFs to accumulate in LAMP1$^+$ and VPS35$^+$ compartments (N = 1 representative experiment out of 2).

(K) Immunostaining for VPS35 (magenta), LAMP1 (yellow), and EEA1 (cyan) in PSEN1$^{+/+}$ or PSEN1$^{-/-}$ DIV 14 neurons (scale bars, 10 μm; inset 5 μm).

(L–P) Size of EEA1 (L) and LAMP1 (M) compartments (N = 2, normalized to DMSO). (N)–(P) Increased MOC of EEA1 with LAMP1 (N) or VPS35 with LAMP1 (P) underscoring delayed endolysosomal maturation. Note a non-significant VPS35-EEA1 co-localization (O). For all box-and-whiskers graphs: boxes display the 25/75, and the whiskers the 10/90 percentiles. Mann-Whitney tests were applied.

Please cite this article in press as: Bretou et al., Accumulation of APP C-terminal fragments causes endolysosomal dysfunction through the dysregulation of late endosome to lysosome-ER contact sites, Developmental Cell (2024), https://doi.org/10.1016/j.devcel.2024.03.030

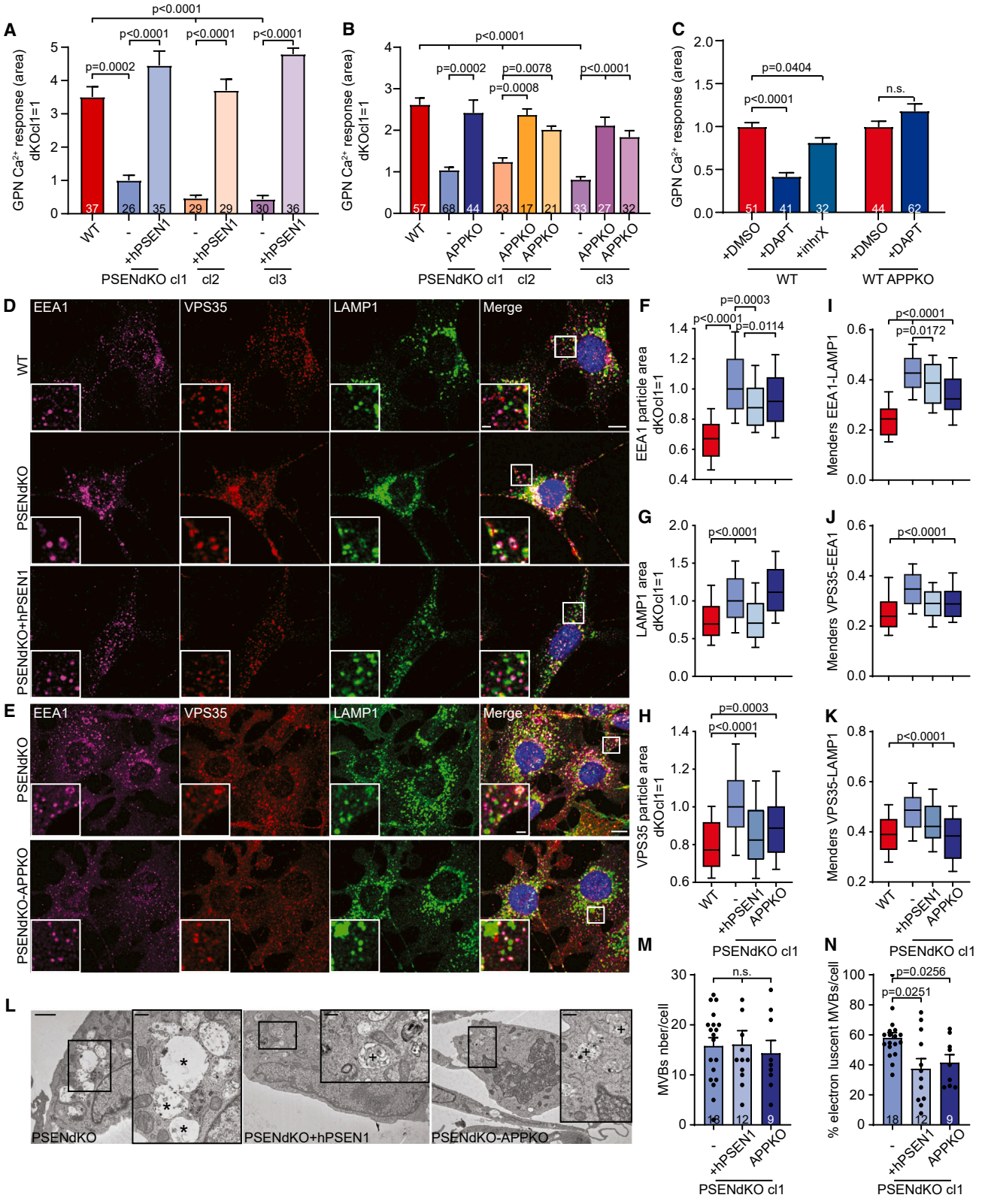

Figure 3. APP deficiency normalizes endolysosomal defects

(A) Lysosomal Ca^{2+} levels are reduced in PSENdKO clones and restored when rescued by hPSEN1 ($N = 3$, normalized to PSENdKO).

(B) APP-KO restored lysosomal Ca^{2+} in PSENdKO cells ($N > 2$).

(legend continued on next page)

Please cite this article in press as: Bretou et al., Accumulation of APP C-terminal fragments causes endolysosomal dysfunction through the dysregulation of late endosome to lysosome-ER contact sites, Developmental Cell (2024), https://doi.org/10.1016/j.devcel.2024.03.030

surface-localized CTxB and Cav1 rapidly internalized and relocated to a perinuclear compartment,[39] irrespective of the presence of PSEN1 and underscoring that endocytosis is not affected by PSEN deficiency (Figure S3C). Replating cells on fibronectin failed to restore the polarized distribution of CTxB and Cav1 at the cell surface in PSENdKO cells (Figures S3C–S3E), whereas this was rescued by hPSEN1 reintroduction or APP depletion. This prolonged intracellular clustering in PSENdKO cells indicates therefore a defect in endosomal recycling. Taken together, our data underscore the notion that the major endosomal and lysosomal defects observed in PSENdKO cells can be traced back to APP expression. We, therefore, addressed next how APP mechanistically interferes in these processes.

Both APP α- and βCTFs induce endolysosomal defects

We first stably re-introduced full-length APP695, αCTFs (C83), or βCTFs (C99) in PSENdKO-APPKO cells (Figure S4A). Whereas previous studies[17,18,40] contributed toward the idea of a selective role for APP-βCTFs in inducing Rab5-positive endosomal enlargements, we surprisingly found that both α- and βCTFs were equally responsible for the appearance of enlarged EEA1- and VPS35-positive compartments and an increased co-localization of early and late endosomal markers (Figures 4A–4E and S4A–S4C). Thus, the endolysosomal collapse as seen in PSENdKO and DAPT-treated WT cells may arise to a similar extent from the accumulation of different types of APP-CTFs. Correspondingly, re-expression of APP-α- or βCTFs led to a defective endosomal recycling (Figures S4D and S4E) and, like APP695, significantly impacted lysosomal Ca^{2+} homeostasis, similar to PSENdKO cells (Figure 4F).

Endolysosomal defects require the membrane anchoring of the AICD

As we have shown that the N terminus of APP-CTFs is not a differentiating factor in the observed endolysosomal defects, we next focused on the AICD (Figure 4G). Whereas γ-secretase processing initiates downstream (nuclear) signaling, e.g., in the case of Notch, intramembrane proteolysis of other substrates may be required to abrogate their functioning.[41] The fact that an increasing number of reports identify APP-CTF accumulation as the incentive for a broad range of endolysosomal defects points to (1) APP-CTFs instigating cell signaling and (2) cells needing to keep the APP-CTF levels in check through γ-secretase processing. To test this hypothesis, we stably expressed AICD modified at its N terminus with a myristoylation motif (mAICD), ensuring membrane anchoring[42,43] in our PSENdKO/APPKO cells (Figure 4G). Expression of mAICD fully recapitulated endolysosomal defects observed in PSENdKO as well as in APP-CTF-rescued PSENdKO-APPKO cells. In particular, mAICD expression decreased lysosomal Ca^{2+} content (Figure 4O), promoted enlargement of EEA1-, VPS35-, and LAMP1-positive compartments, along with an increased VPS35-EEA1 and VPS35-LAMP1 co-localization, showing a delay/collapse in endolysosomal maturation (Figures 4B–4N and S5A) as well as an endosomal recycling defect (Figures S5B and S5C). Interestingly, stable expression of a mutant variant of mAICD, with the Tyr residues of the YENPTY motif mutated to Ala, did not induce endolysosomal defects, including lysosomal Ca^{2+} dyshomeostasis (Figures 4H–4O). These data support the finding that the APP-CTF is the active signaling fragment of APP and that its levels need to be homeostatically controlled through γ-secretase.

The YENPTY is a key motif for the binding of adaptor proteins such as SorLA,[44] Fe65,[45] X11/Mint,[45] and Dab1,[46] as well as the FYVE-type zinc finger-containing phosphoinositide kinase PikFYVE,[47] indicating the pleiomorphic nature of downstream signaling. Part of the observed effects could originate from the re-location of signaling-defective mAICD from a pronounced endolysosomal localization to the cell surface (Figure 4H). However, endolysosomal defects similar to those observed in PSENdKO cells are observed in cells expressing a PikFYVE dominant negative mutant[48] or in WT cells treated with the PikFYVE inhibitor YM201636 (Figure S5D). Likewise, inhibiting Abl kinase in PSENdKO cells, using Imatinib,[49] alleviated the delay in endolysosomal maturation, as evidenced from the lowered VPS35-LAMP1 co-localization and restored dose-dependent lysosomal Ca^{2+} content (Figures S5E–S5I). Improved sorting and recycling resulted in a significant decrease of APP-CTFs in VPS35-positive organelles (Figure S5G), albeit this was not observed for LAMP1-positive LE/Lys (Figure S5F). Altogether, this indicates that inhibition of signaling emanating from APP-derived fragments alleviates endolysosomal defects, mostly through restoration of cargo recycling.

Reduced lysosomal Ca^{2+} content originates from an altered communication with the ER

Whereas we showed that chronic γ-secretase inhibition identified a decreased lysosomal Ca^{2+} content at the root of endolysosomal dyshomeostasis, the data above suggest it may originate from a sustained signaling from membrane-tethered AICD fragments. To scrutinize this, we first addressed the origin of the lysosomal Ca^{2+} dyshomeostasis. In contrast to previous reports,[23,50] we could not relate this defect to an overactivation

(C) Lysosomal Ca^{2+} is reduced following DAPT or inhibitor X (4 days), but not in APPKO cells ($N = 3$, normalized to DMSO).
(D and E) Immunostaining for VPS35 (red), EEA1 (magenta), and LAMP1 (green) in WT, PSENdKO, and PSENDKO+hPSEN1 cells (D), and PSENdKO versus PSENdKO-APPKO cells (E) (scale bars, 10 μm; insets 2 μm).
(F–H) Re-expression of hPSEN1 or APP depletion in PSENdKO normalized the size of $EEA1^+$ (F) and $VPS35^+$ (H) endosomes. LAMP1 area normalized in hPSEN1-rescued cells, but not following APP depletion (G) ($N \geq 2$, with $n = 73$, 161, 66, and 75 cells, F; $n = 150$, 243, 160, and 75 cells, G; $n = 138$, 200, 145, and 75 cells, H).
(I–K) Endolysosomal collapse shown by increased MOC for EEA1 with LAMP1 (I), VPS35 with EEA1 (J), and VPS35 with LAMP1 (K) in PSENdKO cells, which is restored in hPSEN1 rescue or APP depletion ($N \geq 2$ with $n = 73$, 152, 66, and 64 cells in I; $n = 73$, 152, 66, and 64 cells in J; $n = 150$, 234, 158, and 64 cells in K).
(F)–(K) Data were normalized to PSENdKO.
(L–N) TEM of PSENdKO cells with enlarged electron-lucent MVBs, containing no/few intraluminal vesicles compared with hPSEN1-rescued or APP-depleted cells (* empty MVBs, + normal MVBs; scale bars, 2 μm; inset 500 nm). (M and N) Quantification of (L) showed unaltered MVB numbers per cell but increased electron-lucent MVBs in PSENdKO cells (mean ± SEM). Multiple ANOVA Kruskal-Wallis with Dunn's post hoc test, except the Mann-Whitney test for (M) and (N). For all box-and-whiskers graphs: boxes display the 25/75, and the whiskers the 10/90 percentiles.

Please cite this article in press as: Bretou et al., Accumulation of APP C-terminal fragments causes endolysosomal dysfunction through the dysregulation of late endosome to lysosome-ER contact sites, Developmental Cell (2024), https://doi.org/10.1016/j.devcel.2024.03.030

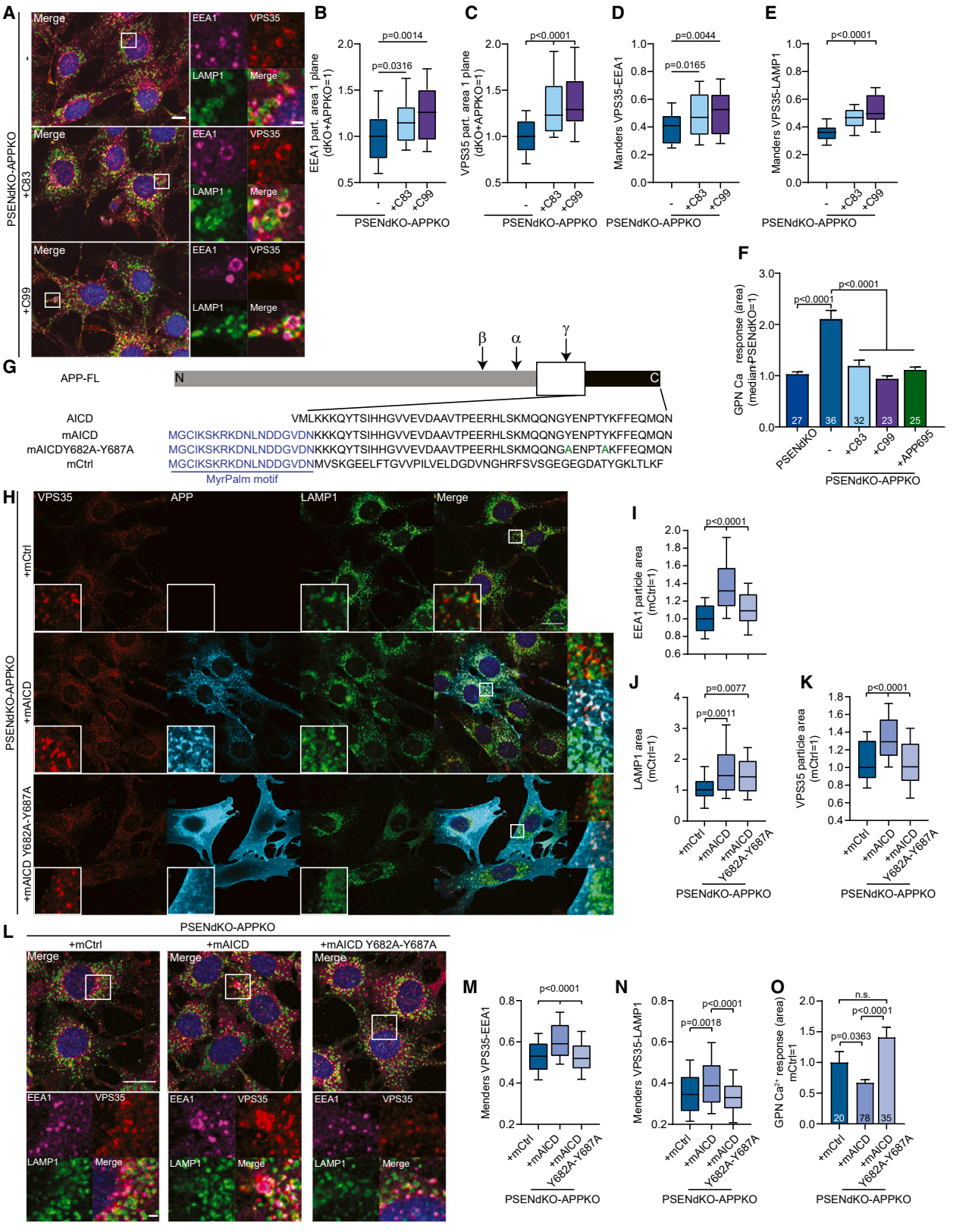

(legend on next page)

of the lysosomal Ca^{2+} channel transient receptor potential mucolipin 1, also called mucolipin-1 (TRPML1). First, a challenge with the TRPML1 agonist—MLSA1—did not reveal an overactivation of the channel in three independent PSENdKO clones (Figure 6A). Second, we generated a KI mouse model wherein TRMPL1 was endogenously tagged with the Ca^{2+} sensor Gcamp6S and crossed this line with our PSEN1KO mouse model. Primary neurons derived from PSEN1 KO/KO Gcamp6S-TRPML1 KI/KI embryos did not display an increased lysosomal Ca^{2+} response when challenged with MLSA1, as previously reported,[23] whereas the GPN elicited Ca^{2+} response remained reduced as compared with their WT/WT counterparts (Figure S6B).

Another potential source of the lysosomal Ca^{2+} defect could originate from a failed communication between the ER and lysosomes.[51,52] We therefore assessed the Ca^{2+} refilling of the lysosomes from the ER in our different cell lines (Figures 5A, S6C, and S6D).[51] Fura2-AM-loaded cells were repeatedly challenged with GPN in the absence of extracellular Ca^{2+}, allowing the emptying of lysosomal Ca^{2+}, alternating with "rest phases" in the presence of extracellular Ca^{2+}, to allow lysosomes to reseal and refill from the ER (Figures S6C and S6D). PSENdKO cells displayed a significantly decreased lysosomal Ca^{2+} refilling, which was restored upon stable hPSEN1 re-expression or when APP was additionally knocked out (Figures 5A and S6C). These findings point to a derailed ER-to-lysosome Ca^{2+} transfer, which occurs through LE/Lys-ER MCSs.[51–53] We, therefore, investigated next whether APP-CTFs interfered within or near LE/Lys-ER MCSs. We performed super-resolution Airyscan imaging of PSENdKO and PSENdKO-APPKO cells stably rescued with APP-βCTF (C99) or mAICD and co-transfected with GFP-Sec61b (to mark the ER; Figures 5B–5D, S6E, and S6F). APP and/or APP-CTFs often appeared clustered on the limiting membrane of LAMP1-positive LE/Lys and in close apposition to GFP-Sec61b$^+$ ER membranes, as shown by the respective line scans (Figures 5B–5D), indicating their localization in LE/Lys-ER MCSs. APP immunoreactivity did not overlap with GFP-Sec61b, making APP-CTFs exert their role in MCSs from the side of LE/Lys. Similar close appositions in the range of 80–120 nm, typical for MCSs, were observed in mAICD-expressing cells (Figure 5D). To further validate this, we promoted the formation of LE/Lys-ER MCSs through overexpression of VAPB and Stard3,[54] leading to the prominent co-localization of APP/APP-related fragments with Stard3 in LE/Lys-ER MCSs (Figures S6G and S6H). Exogenous expression of Stard3 in DAPT-treated primary hippocampal neurons likewise resulted in an accumulation of APP-CTFs in Stard3-positive domains juxtaposed with the ER, underscoring a conserved feature of APP-CTFs (Figure S6I). To further confirm the localization of APP-CTFs to these MCSs, we treated cells with a hypotonic (5% DMEM in water) solution, which results in the rapid vacuolization of intracellular compartments without affecting inter-organellar contacts.[55] The formation of large intracellular vesicles (LICVs) makes MCSs more visible, facilitating co-localization analysis. Hypotonic treatment of PSENdKO-APPKO cells, transfected with mCherry-Sec61b and either APP-YFP (Figure 5E) or C99-GFP (Figure 5F), resulted in APP-positive LICVs contacting ER-derived LICVs and with APP/APP-CTFs being frequently enriched at these contact sites, within a similar range of 80–120 nm to mCherry-Sec61b$^+$ LICVs (Figures 5B and 5C and line scans herein). These data therefore demonstrate the localization of APP-CTFs to LE/Lys-ER MCSs, where they may modulate ER-to-lysosome Ca^{2+} transfer. As a control, line scans of triple-immunostained PSENdKO and PSENdKO-APPKO cells rescued with C99 with HSP60 did not reveal close appositions with mitochondria, reminiscent of MCSs (Figures 5G and 5H). Likewise, live imaging of cells treated with hypotonic medium showed much larger distances between APP- and MitoTracker-positive LICVs (Figures 5I and 5J), arguing against the presence of APP-C99 in mitochondria-associated membranes (MAMs or ER-mitochondria MCSs), as reported before.[56,57] To scrutinize whether APP-βCTF (C99) accumulation is responsible for mitochondrial defects observed in PSEN-deficient cells, we tested mitochondrial fitness using a Seahorse metabolic analysis (Figures S6J–S6O). PSENdKO MEFs exhibited a significant decrease in their maximal respiration and ATP production; these metabolic abnormalities were restored in hPSEN1-rescued but not in PSENdKOxAPPKO MEFs (Figures S6J–S6L). Regarding oxygen consumption rate (OCR) and basal respiration, re-expression of PSEN1 partially restored levels to WT MEFs, whereas depletion of APP did not (Figures S6M and S6N). Only the deficiency in the spare respiratory capacity (SRC) was found to be rescued by APP deficiency. Overall, and in support of a lack of localization of APP-C99 to

Figure 4. Endolysosomal defects are caused by membrane-anchored APP intracellular domains

(A) Immunostaining for EEA1 (magenta), VPS35 (red), and LAMP1 (green) in PSENdKO-APPKO cells expressing no, α-(C83), or β(C99) CTFs (scale bars, 10 μm; insets 2 μm).

(B and C) Re-introducing α/βCTFs resulted in enlarged EEA1$^+$ (B) and VPS35$^+$ (C) endosomes ($N = 2$, normalized to PSENdKO cells, with $n = 45$, 49, and 50 cells [left to right]).

(D and E) MOC showed increased co-localization of VPS35 with EEA1 (D) or LAMP1 (E) upon CTF expression in PSENdKO-APPKO cells ($N = 2$, with $n = 47$, 49, and 50 cells).

(F) CTF expression in PSENdKO-APPKO cells decreased lysosomal Ca^{2+} as in PSENdKO cells ($N = 2$ experiments, mean ± SEM, normalized to PSENdKO). Multiple ANOVA Kruskal-Wallis with Dunn's post hoc test were applied.

(G) Amino acid sequence of control (mCtrl) and myristoylated AICD (mAICD; mutations in green).

(H) Immunostaining for VPS35 (red), APP (cyan), and LAMP1 (green) in PSENdKO-APPKO cells rescued with mCtrl, mAICD, or mutant mAICD (which re-localized to the plasma membrane) (scale bars, 10 μm; insets 5 μm).

(I–K) Re-expression of mAICD caused enlarged EEA1$^+$ (D), LAMP1$^+$ (E), and VPS35$^+$ (F) positive compartments ($N = 3$ with $n = 59$, 65, and 70 cells [left to right] for D, and $n = 46$, 57, and 52 cells for E and F; data normalized to mCtrl).

(L) Immunostaining for EEA1 (magenta), VPS35 (red), and LAMP1 (green) in AICD-rescued cells (scale bars, 20 μm; insets 2 μm).

(M and N) MOC showed increased co-localization of VPS35 with EEA1 (M) or LAMP1 (N) in mAICD-expressing cells ($N \geq 3$ with $n = 59$, 65, and 70 cells in M, $n = 106$, 122, and 125 cells in N).

(O) Reduced lysosomal Ca^{2+} in mAICD- but not mutant mAICD-expressing cells ($N = 2$, normalized to mCtrl; mean ± SEM). Multiple ANOVA Kruskal-Wallis with Dunn's post hoc test, except the Mann-Whitney test for (I). For all box-and-whiskers graphs: boxes display the 25/75, and the whiskers the 10/90 percentiles.

Please cite this article in press as: Bretou et al., Accumulation of APP C-terminal fragments causes endolysosomal dysfunction through the dysregulation of late endosome to lysosome-ER contact sites, Developmental Cell (2024), https://doi.org/10.1016/j.devcel.2024.03.030

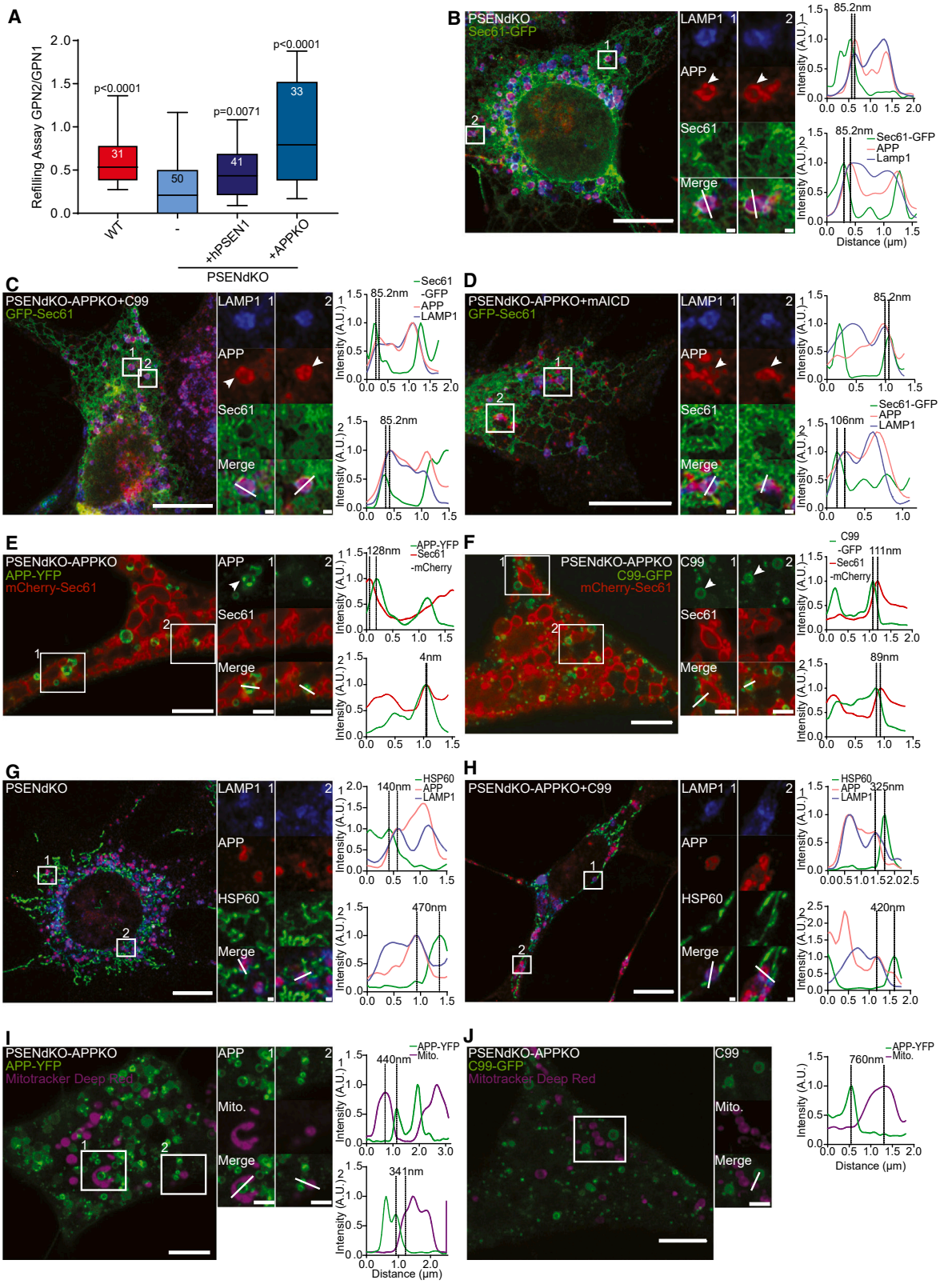

(legend on next page)

ER-Mito MCSs, these data support our conclusion that, in PSENdKO cells, APP expression is not significantly contributing to the observed mitochondrial metabolic defects.

Accumulation of membrane-tethered APP fragments affects LE/Lys-ER MCS morphology and LE/Lys dynamics

We next investigated whether the increased localization of APP-CTFs impacted LE/Lys-ER MCS morphology. Visualization of the ER by TEM was facilitated by co-expressing a KDEL sequence fused to a horseradish peroxidase and myc-tag (HRP-myc-KDEL), followed by 3′ 3-Diaminobenzidine tetrahydrochloride (DAB) treatment.[58] First, PSENdKO cells display increased numbers of electron-lucent vesicles (red asterisk in Figure 6A; see also Figure S3A for unrelated PSENdKO cells), likely reflecting a delayed maturation to MVBs. As expected, this phenotype disappeared in hPSEN1-rescued PSENdKO and PSENdKO-APPKO cells but re-appeared when the latter cells were stably rescued with mAICD (Figure 6A). Whereas the HRP-reactive ER of both PSENdKO and PSENdKO-APPKO-mAICD cells generally appeared more swollen, in addition, many enlarged contacts of the ER were noticeable with LE/MVBs, sometimes largely encapsulating them (Figure 6A, zoomed insets). Reintroducing hPSEN1 in PSENdKO or depleting APP herein significantly reduced lengths, indicating a normalization of MCSs (see also quantification in Figure 6A).

We further reasoned that the enlarged contacts of ER with LE/Lys might also affect other aspects of LE/Lys, including motility. To test this, we used lattice-structured illumination microscopy (SIM; Zeiss Elyra-7) and compared the dynamics of LysoTracker-labeled acidic organelles in the different cell lines. PALMtracer (see STAR Methods) was used to track individual organelles and to quantify changes in the time-correlated mean-squared displacement (MSD). This approach allows one to distinguish different types of motility from random motion.[2] In agreement with the observed enlarged LE/Lys-ER contacts, only cells accumulating or expressing membrane-tethered AICD fragments (either CTFs or mAICD) display a significantly increased proportion of immobile tracks, reminiscent of less-motile organelles (Figures 6B and 6E). Concordantly, we observed a reduction in the MSD and diffusion coefficients (Figures 6C and 6D). The decreased motility correlated with longer retention of the LysoTracker Red-labeled organelles on the ER; indicated by the higher co-localization of these organelles (Figures 6F and 6G; Videos S1–S5).

Promoting cholesterol egress largely restores endolysosomal demise in PSEN-deficient cells

Thus far, we showed that a decreased lysosomal Ca^{2+} content of PSEN-deficient cells can be functionally linked to the accumulation of APP-CTFs or mAICD converging with altered LE/Lys-ER MCSs. Moreover, both a decrease in lysosomal Ca^{2+} and cholesterol accretion are the two primary events preceding endolysosomal collapse when chronically inhibiting γ-secretase. Therefore, we first reasoned that preventing lysosomal Ca^{2+} release might prevent downstream endolysosomal defects. LE/Lys contain different Ca^{2+} transporters, including TRPML1 and TPC2 (two-pore channel 2).[59] Chronic treatment of PSENdKO MEFs, or PSEN1$^{-/-}$ hippocampal neurons with the TPC2-inhibitor, NED-19 (400 nM), rescued LE/Lys Ca^{2+} release in a manner reminiscent of WT cells (Figures S7I and S7J). NED-19 also reduced the LAMP1- and VPS35-positive area (Figures S7A, S7B, S7D, and S7E) and decreased endolysosomal collapse, as shown by the lowered co-localization of LAMP1 with EEA1 and VPS35, although the latter not significantly (Figures S7F and S7G). As we showed that APP/APP-CTF accretion in LE/Lys is sufficient to induce endolysosomal demise, the failure of NED-19 to reduce its localization in LAMP1-positive compartments (Figure S7H) might explain the failure of NED-19 to fully rescue more downstream effects of decreased LE/Lys Ca^{2+} storage. Besides lysosomal Ca^{2+} dysfunction, PSEN1KO cells also share cholesterol accumulation in LE/Lys with NPC1KOs,[59–62] although more modestly (Figure S8A). We therefore wondered whether counteracting cholesterol accretion could alleviate endolysosomal demise in PSEN-deficient cells. Free cholesterol, as measured by filipin staining, accumulated in LAMP1 compartments of PSENdKO and PSENdKO-APPKO cells rescued with APP-CTFs or mAICD (Figures 7A and 7B). Within these organelles, filipin is clearly co-localized with APP-CTFs and mAICD (Figures 7A–7D). Depleting APP in a PSENdKO background or re-expression of mutant mAICD reverted the accumulations back to WT levels. Hence, we wondered whether alleviating the burden of cholesterol in LE/Lys could correct lysosomal Ca^{2+} defects. We treated PSENdKO cells with OSW-1, an inhibitor of OSBP and ORP4L, counteracting the sequestration of cholesterol from the ER to the lysosome.[61–63] Treatment did not decrease lysosomal cholesterol staining nor did it rescue lysosomal Ca^{2+} dysfunction of PSENdKO cells (Figures S8B and S8C). This indicates that the cholesterol accumulated in LE/Lys does not originate from an ER pool. Alternatively, we induced egress of lysosomal cholesterol through overexpression of NPC1 or treatment with 2-hydroxypropyl-γ-cyclodextrin (HPγCD), a

Figure 5. APP-CTF- and mAICD-induced lowered lysosomal Ca^{2+} originates from altered LE/Lys-ER contacts

(A) Lysosomal Ca^{2+} refilling is impaired in PSENdKO cells but normalized in hPSEN1-rescued or APP-depleted PSENdKO cells (N = 3, 5, 3, and 2).

(B–D) Immunostaining for LAMP1 (blue) and APP (red) in GFP-Sec61b transfected cells. Airyscan resolution of MCSs in PSENdKO (B) versus C99- (C) and mAICD-rescued (D) PSENdKO-APPKO cells (scale bars, 10 μm; insets 0.5 μm).

(E and F) Hypotonic treatment of PSENdKO-APPKO cells transfected with mCherry-Sec61b and APP-YFP (E) or C99-GFP (F). Enlarged APP$^+$ or C99$^+$ organelles closely contact ER (see inset and line scans; scale bars, 5 μm; inset 2 μm).

(G and H) Airyscan imaging of LAMP1 (blue), APP (red), and HSP60 (green) in PSENdKO (G) or PSENdKO-APPKO expressing C99 (H) cells (scale bars, 10 μm; insets 0.5 μm).

(I and J) Hypotonic treatment of PSENdKO-APPKO cells transfected with APP-YFP (green, I) or C99-GFP (green, J) and treated with MitoTracker deep red (violet). No APP$^+$ or C99$^+$-enlarged organelles were nearby mitochondria (see inset and line scans; scale bars, 5 μm; inset 2 μm). For the box-and-whiskers graph: boxes display the 25/75, and the whiskers the 10/90 percentiles. Multiple ANOVA Kruskal-Wallis with Dunn's post hoc test.

Please cite this article in press as: Bretou et al., Accumulation of APP C-terminal fragments causes endolysosomal dysfunction through the dysregulation of late endosome to lysosome-ER contact sites, Developmental Cell (2024), https://doi.org/10.1016/j.devcel.2024.03.030

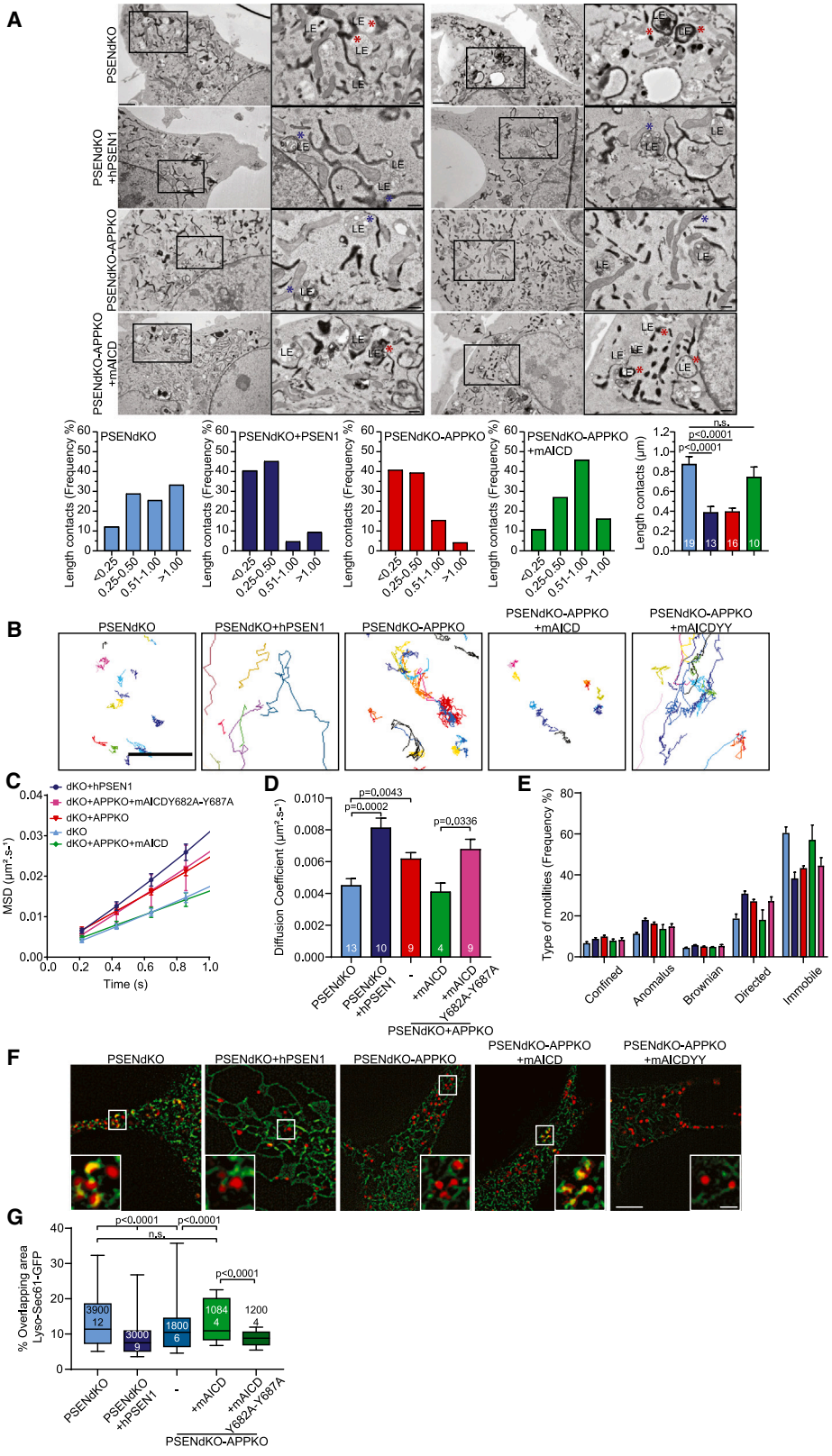

(legend on next page)

drug shown to reduce intracellular free cholesterol and to enhance autophagic activity through the regulation of ER-lysosome MCSs[64,65] (Figures S8D–S8Q). Both NPC1 overexpression and HPγCD treatment strongly reduced the accumulation of membrane-tethered APP fragments in the LAMP1-positive LE/Lys of PSENdKO cells (Figures S8D and S8E, also visible in Figures S8F, S8K, S8L, and S8O), and fully restored lysosomal Ca^{2+} content (Figure 7E). Of note, these treatments also partially restored the endolysosomal maturation, as seen by the reduced EEA1 area and decreased co-localization of VPS35 with either EEA1 or LAMP1 (Figures S8H–S8J, S8L, S8M, S8P, and S8Q). In conclusion, treatments that promoted cholesterol efflux from the LE/lysosomes, but not from the ER, relieved both lysosomal Ca^{2+} and endolysosomal defects observed in PSEN-deficient cells.

DISCUSSION

In this manuscript, we elucidated how elevated levels of APP-CTFs mechanistically contribute to endolysosomal demise, observed in PSEN-deficient cells and neurons or upon γ-secretase inhibition. Our data establish a functional link between APP processing and maintaining the proper balance of lysosomal Ca^{2+} through an ER Ca^{2+} refilling pathway. Additionally, APP-CTFs clustered on the membranes of LE/Lys, proximal to or within MCSs with the ER. Abnormal accumulation of APP-CTFs, seen in PSEN/γ-secretase-deficient or DAPT-treated cells, feeds a prolonged signaling cascade originating from APP's cytosolic domain, disrupting inter-organellar communication and impairing ER-to-LE/Lys Ca^{2+} refilling. We propose that proteolysis of APP-CTFs on LE/Lys is essential for safeguarding homeostasis in LE/Lys-ER communication. Notably, similar data were obtained in both non-neuronal cells and primary hippocampal neurons, underscoring conserved mechanisms.

In the context of PSEN deficiency, our data do not support a primary causal role for v-ATPase in the observed lysosomal defects, contrary to previous research.[22] In independent PSENdKO clones, we observed no alterations in the activity of the lysosomal localized v-ATPase (Figure S2B) and only minor lysosomal pH changes, but within the physiological range of 4.5–5.0,[34] in agreement with previous reports.[24,26] However, Im and colleagues recently reported that excess APP-βCTF, particularly a phosphorylated form, disrupted v-ATPase function via direct interaction with the Voa1 subunit.[28] But also here, the impact on lysosomal pH was relatively modest, with a maximum deviation of 0.5 pH units, slightly above the physiological range. We argue that such changes result from other early events, such as decreased lysosomal Ca^{2+} levels and changes in lipid composition (Figures 1, 2, and 7) affecting endosomal recycling and ultimately resulting in enlarged early endosomal compartments. Further, the increased co-localization of lysosomal and endosomal markers indicated a progressive collapse of the endolysosomal compartment. Our study is the first to report the chronology of the endolysosomal collapse initiated by a lysosomal Ca^{2+} deficit following γ-secretase inhibition. Previous studies focused primarily on individual endosomal or lysosomal defects without directly linking them to PSEN/γ-secretase loss of function, either through KO or FAD-associated mutations. Thus, previously reported defects, such as Rab5 overactivation and early endosomal enlargement,[17–19] recycling distortion[66] and autophagy dysfunction,[18] may be later events in endolysosomal demise, downstream of LE/Lys dysfunction. Alternatively, studies using overexpression or knockdown/KO of key endosomal regulators have demonstrated causal relationships, although such dramatic alterations in expression can themselves lead to endolysosomal collapse,[67–69] which is mechanistically distinct from our observations in PSEN-inactivated cells and neurons. For instance, the effects of constitutively active Rab5-Q79L on endosomal collapse are well-documented *in vitro*, and Rab5 overactivation (through overexpression) drives endosomal dysfunction *in vivo*, resulting in a neurodegenerative cascade.[70]

Regarding VPS35, limited data exist related to PSEN deficiency, although decreased expression levels are noted in an AD context.[71] Enlarged VPS35-positive compartments observed in PSEN-deficient cells and neurons may stem from recycling failure, akin to when another recycling regulator, ARF6, is depleted.[72] We propose that these recycling defects may originate from lowered LE/Lys Ca^{2+} content and abnormal cholesterol accumulation in LE/Lys, which disrupts fusion and fission events crucial for cargo recycling. This defect in recycling appears to affect raft-associated proteins and lipids selectively, as evidenced by our suspension-adhesion assay, and consistent with the selective depletion of raft-associated proteins and lipids in isolated plasma membranes of PSENdKO cells.[73] Therefore, a re-activation of recycling could potentially be targeted as well to restore endolysosomal collapse.[74]

Our findings provide another insight into APP-mediated signaling, challenging previous notions regarding the function and localization of APP-CTFs. First, we demonstrate that it is abrogation rather than the initiation of downstream signaling of APP that is crucial for maintaining endolysosomal homeostasis. This is not the case for substrates such as Notch, N-cadherin, and ErbB4, where γ-secretase cleavage is integral to key downstream signaling mechanisms.[41,75–78] Second, contrary to

Figure 6. Membrane-tethered APP fragments affect LE/Lys-ER MCS morphology and LE/Lys dynamics

(A) PSENdKO and PSENdKO-APPKO cells expressing mAICD displayed extended LE/Lys-ER contacts, up to encapsulated LE/Lys (right images). MCS lengths (as mean ± SEM, lower row) normalized in hPSEN1-rescued or APP-depleted PSENdKO cells, or PSENdKO-APPKO cells expressing mutant mAICD (blue and red * indicate short and long contacts; scale bars, 2 μm; inset 500 nm).

(B) Representative color-coded tracks of LysoTracker in aforementioned cell lines (scale bars, 1 μm).

(C–E) MSD plot over time revealed decreased organelle motility in PSENdKO and mAICD-expressing PSENdKO-APPKO cells, resulting in reduced diffusion coefficients (D) and a shift from directed to immobile motilities (E). (C–E: n = 13, 10, 9, 4, and 9 cells, from left to right, mean ± SEM).

(F) Representative image of LysoTracker$^+$ organelles and GFP-Sec61b$^+$ ER (scale bars, 5 μm; inset 1 μm).

(G) Percentage overlap of (F), including the number of frames and corresponding cell numbers. For (A) and (C)–(E), mean ± SEM. Mann-Whitney test was applied and, for (A) and (G), one-way ANOVA and multiple ANOVA Kruskal-Wallis with Dunn's post hoc test. For the box-and-whiskers graph: boxes display the 25/75, and the whiskers the 10/90 percentiles.

Please cite this article in press as: Bretou et al., Accumulation of APP C-terminal fragments causes endolysosomal dysfunction through the dysregulation of late endosome to lysosome-ER contact sites, Developmental Cell (2024), https://doi.org/10.1016/j.devcel.2024.03.030

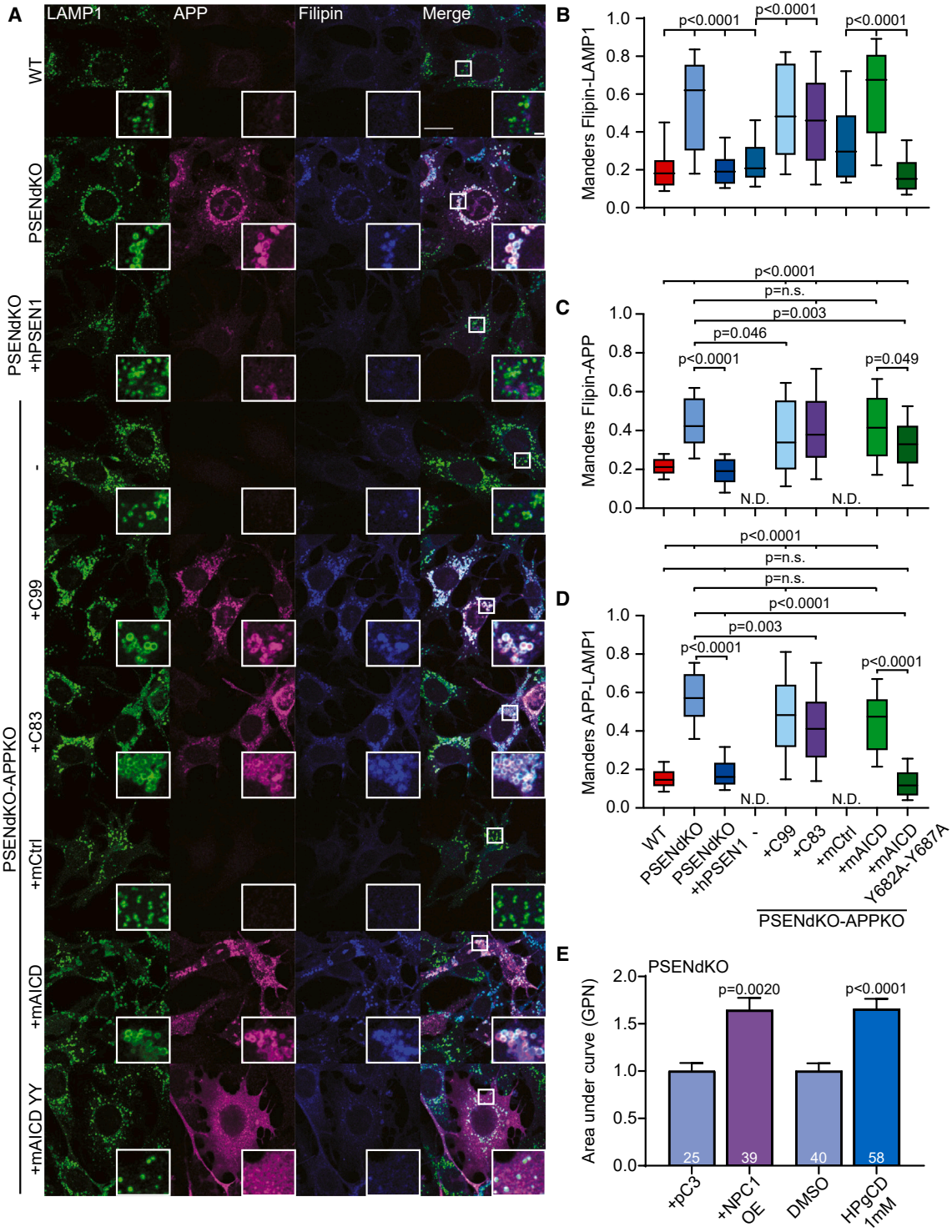

Figure 7. Cholesterol egress corrects lysosomal Ca^{2+} defects

(A) Immunostaining for LAMP1 (green), APP (magenta), and filipin (blue).

(B–D) MOC of filipin-LAMP1 (B), filipin-APP (C), and APP-LAMP1 (D). (B–D: $N = 2$, with $n = 71$, 80, 61, 65, 73, 46, 78, and 67 cells, multiple ANOVA Kruskal-Wallis with Dunn's post hoc test.)

(E) Overexpressing NPC1-FLAGI or treatment with 2-hydroxypropyl-γ-cyclodextrin (HPγCD, 1 mM, 4 days) alleviated lysosomal Ca^{2+} defects in PSENdKO ($N \geq 2$ experiments, mean ± SEM; Mann-Whitney test). For all box-and-whiskers graphs: boxes display the 25/75, and the whiskers the 10/90 percentiles.

Please cite this article in press as: Bretou et al., Accumulation of APP C-terminal fragments causes endolysosomal dysfunction through the dysregulation of late endosome to lysosome-ER contact sites, Developmental Cell (2024), https://doi.org/10.1016/j.devcel.2024.03.030

recent studies,[17–20] we show that both α- and β-cleaved APP-CTFs induced endolysosomal defects. The emphasis on βCTF may originate from neuronal cultures having predominant amyloidogenic processing, overshadowing the subtler effects of increased αCTF levels,[17,18] or overexpression strategies.[20] Further, APP-βCTF can also be processed to αCTFs,[79] blurring the assignment of specific roles to α- or βCTFs. More importantly, membrane-tethering of the AICD fragment was sufficient to reproduce endolysosome defects in combined PSEN- and APP-deficient cells, questioning the existence of a direct nuclear signaling role for AICD, as proposed previously.[80–84]

APP-mediated downstream signaling is largely regulated through its YNPTY motif, with critical mutations abolishing the effects of mAICD on endolysosomal homeostasis (Figures 4 and 7). Inhibiting Abl kinase through Imatinib significantly rescued endolysosomal defects in PSENdKO cells (Figures S5E–S5H), supporting a direct contribution of Abl-mediated downstream signaling on LE/Lys. These findings align with earlier studies linking APP-CTF signaling to neuronal functions. Human APP and its *Drosophila* ortholog, APP-like or APPL, induce axonal arborization through the interaction with Abl kinase,[85] whereas APP-CTF signaling has been linked to wnt signaling.[38] APP-CTFs have been shown to activate cAMP/PKA through binding to Gαs and initiating the signaling of the cAMP response element-binding protein (CREB) in the context of axonodendritic outgrowth regulation in an *in vivo* FAD-PSEN1 KI model.[42,86] Other studies have linked AICD/APP to an indirect activation of Fe65.[87,88] Further investigation is warranted to identify cell-type-dependent signaling pathways downstream of APP-CTFs modulating LE/Lys-ER MCS function.

Super-resolution microscopy revealed domains on LE/Lys enriched for APP and APP-CTFs closely opposed to ER membranes, reminiscent of LE/Lys-ER MCSs. This finding was more pronounced in hypotonic medium maintaining MCS integrity. No APP/APP-CTFs were found in mitochondria-ER MCSs, contrasting previous reports,[57,89,90] but which may be possibly biased by biochemical analysis of isolated MAMs. The combined extraction and sonication procedures inherent in MAM isolation may herein generate artifacts, including contaminations with MCS fragments from other origin. In other cases, overexpression of APP/APP-CTFs was often used,[57,89,91] but APP-CTF overexpression is known to saturate the secretory route, generating compartmental collapse and compromising reliable interpretations. Additionally, recent evidence demonstrated that γ-secretase assembly concludes after ER-exit,[92] making the ER-localized generation of APP-CTFs (and MAM association) unlikely. In our study, most PSEN-deficiency-linked defects in mitochondrial metabolism could also not be rescued by APP KO, arguing for an indirect causal origin (Figures S6J–S6O). Herein, only the SRC (which could be seen as a determinant of mitochondrial fitness)[93] and the extracellular acidification rate (ECAR; linked to glycolysis) were rescued, underlining only a minor role of APP in the handling of stress. The exact contribution of APP and its fragments requires further investigation.

However, localization of APP/APP-CTFs in LE/Lys-ER does not necessarily contradict observed mitochondrial dysfunctions in PSEN-deficient cells[94–97] or AD contexts.[89,98–100] Lysosomes and mitochondria form functional MCSs, regulating lysosomal and mitochondrial networks bidirectionally, potentially explaining their concurrent dysfunction in neurodegenerative diseases.[101] For example, related to Parkinsonism, deficiency of the lysosomal polyamine transporter ATP13A2 potentiates ROS accumulation, which affects mitochondrial functioning.[102] Lysosomal dysfunction in lysosomal storage diseases alters autophagy/mitophagy, resulting in the accumulation of dysfunctional/damaged mitochondria.[103] In late onset AD (LOAD), failure of the lysosomal exonuclease phospholipase 3 (PLD3) to degrade mitochondrial DNA leads to primary lysosomal/autophagy dysfunctions and cytosolic accumulation of dysfunctional mitochondria.[104]

Although more subtle in PSEN/γ-secretase deficiency, the sequence of lysosomal to endosomal defects resembles NPC1 deficiency, where reduced lysosomal Ca^{2+} content is also an initial sign of lysosomal dysfunction.[60] Sphingosine accumulation in acidic compartments triggers this reduction, followed by cholesterol and glycosphingolipids storage. Although we did not investigate sphingosine 1, its accumulation has already been described in an AD context.[105] Studies by Davis and Lim further described a cholesterol egress through NPC1 to involve MCSs as well,[61,62] and likely involves crosstalk with Ca^{2+} refilling from the ER.[106] However, the failure of OSW-1 to rescue cholesterol accumulation in PSEN-deficient cells suggests that the build-up originates elsewhere, unlike what is observed in NPC1KO cells, where it relies on cholesterol transfer from the ER to lysosomes through OSBP.[62] Nevertheless, stimulation of cholesterol egress by NPC1 overexpression or HPγCD treatment decreased cholesterol levels and rescued endolysosomal demise, including lysosomal Ca^{2+} content, possibly through the modulation of ER-LE/Lys MCSs, as in NPC1 KO cells.[62,64,65] In NPC1 KO neurons, cholesterol accumulation disrupted lysosomal trafficking by sequestering motor adaptors, potentially contributing to decreased lysosome motility.[107,108] We show lysosomal motility to be significantly decreased in PSENdKO cells (and rescued upon APP depletion or re-introduction of hPSEN1 [Figure 6]), possibly due to the extended LE/Lys-ER MCSs promoting prolonged interaction, thus hindering motility.

It is noteworthy that we did not recapitulate cholesterol accumulation in PSEN1KO neurons. Although we cannot exclude a role for PSEN2/γ-secretase herein, alternatively, cholesterol accumulation could be cell-type-dependent. Essayan-Perez and Südhof recently showed that pharmacological inhibition or genetic ablation of γ-secretase in primary neurons decreased cholesterol levels, whereas this was not observed in PSEN1-deficient glial cells.[109] Thus, while moderate accumulations of cholesterol in LE/Lys may aggravate endolysosomal dysfunctions in non-neuronal PSENdKO cells, our data support decreased lysosomal Ca^{2+} storage capacity as an early event driving downstream lysosomal and endosomal dysfunctions, consistent across non-neuronal and neuronal cells.[23–25,110]

Herein, our results point to an inefficient Ca^{2+} refilling of LE/Lys from the ER rather than overactivation of a lysosomal Ca^{2+} channel such as TRPML1.[23] The ER has been shown to drive a main route for Ca^{2+} refilling through LE/Lys-ER MCSs.[51] Atakpa et al. demonstrated that IP3 receptors cluster near ER-LE/Lys MCs, facilitating local delivery of Ca^{2+} from the ER to LE/lysosomes.[111] Ca^{2+} delivery occurred in a "piston-like" manner through IP3Rs to present it to a low-affinity lysosomal uptake system. LE/Lys Ca^{2+} uptake depended on the dynamic regulation of ER-LE/Lys

MCSs, which is affected in PSENdKO cells and negatively regulated through APP metabolism. Interestingly, inhibition of v-ATPase did not prevent ER-to-LE/Lys Ca^{2+} refilling activity,[51] whereas sustained inhibition disrupted ER-LE/Lys MCSs.[111] The longer and more stable ER-Lys MCSs in PSENdKO cells thus also argue against pH defects as a primary cause of LE/Lys dysfunction in PSEN-deficient cells.

In PSEN/γ-secretase-inactivated cells and neurons, the absence of Aβ allowed us to identify the toxic contributions of APP-CTFs. The similarity between PSENdKO and FAD-PSEN1-expressing cell models (this study and Kwart et al.[17] and Hung et al.[18]) suggests that most, if not all, observed endolysosomal defects may be attributed to APP-CTF accumulation. Further, endosomal abnormalities are observed early in AD pathology, independent from the build-up of Aβ and before major AD hallmarks appear.[8] Aberrant APP-CTF accumulation may therefore be closer to the onset of AD neuropathogenesis through gradually disrupting lysosomal homeostasis, tipping the balance ultimately to a general endolysosomal collapse and neuronal cell death.[1,74] Although more work is needed, recent studies also report on increased APP-CTF levels in LOAD.[112,113] For instance, LOAD-linked variants in PLD3 significantly delayed autolysosome turnover, resulting in APP-CTF accumulation and aggravating endolysosomal demise.[104]

The critical organellar toxicity of APP-CTFs may have contributed to the failure of clinical trials on γ-secretase inhibitors[114] and could compromise the efficacy of future compounds targeting this enzyme. Our findings support the development of modulators or stabilizers to restore γ-secretase processivity, thereby normalizing APP-CTF turnover. Alleviating the APP-CTF burden could be a promising therapeutic approach in combatting AD, potentially serving as an early biomarker and upfront therapeutic target.[115] Addressing pathogenic mechanisms such as Aβ clearance, tau pathology, and neuroinflammation may not effectively mitigate APP-CTF toxicity unless combined with strategies such as BACE-1 inhibitors.[116] In conclusion, our study underscores the critical role of homeostatic APP processing in LE/Lys-ER MCSs, the failure of which triggers a detrimental cascade leading to a general endolysosomal demise crucial for neuronal survival. It further emphasizes the multifaceted role of γ-secretase, not only as a generator of toxic Aβ but also as a beneficial protease that inactivates APP-CTFs.

Limitations of the study

This study explored the mechanism by which excess APP-CTFs drive endolysosomal dysfunction, using an engineered cell line deficient for both PSENs and APP. The conclusions in our study are limited to PSEN deficiency and need to be extended to FAD-associated mutations in PSEN1 to extrapolate these observations to endolysosomal abnormalities as observed in the AD brain. Herein, follow-up studies in physiologically more relevant AD models, including iPSC-derived human neurons, AD mouse models, and human samples, are required to generalize our main outcomes. Our study provided further support for the critical role of γ-secretase-mediated APP proteolysis in maintaining endolysosomal homeostasis. However, it does not fully exclude the contribution of a γ-secretase-independent role for PSENs herein. Likewise, to what extent γ-secretase heterogeneity, with distinctly composed complexes being co-expressed in the cell, contributes to lysosomal homeostasis is subject to further investigation. Although our research indicates that APP-CTFs, and specifically their cytosolic domain, induce a toxic signaling cascade, the exact downstream signaling pathway(s) and how they modulate LE/Lys-ER contact dynamics remain unknown. Lastly, knocking out APP in PSEN-deficient cells failed to rescue observed defects in mitochondrial fitness, arguing for a yet unknown APP-independent mechanism distorting lysosomal to mitochondrial communication in these cells.

STAR★METHODS

Detailed methods are provided in the online version of this paper and include the following:

- KEY RESOURCES TABLE
- RESOURCE AVAILABILITY
  - Lead contact
  - Materials availability
  - Data and code availability
- EXPERIMENTAL MODEL AND STUDY PARTICIPANT DETAILS
  - Animal
- METHOD DETAILS
  - Antibodies and reagents
  - Drug treatments
  - Plasmids and Cell transfection
  - Generation of stable cell lines
  - Western blotting
  - Calcium dynamics
  - Lysosomal pH measurement
  - Isolation of Late Endosomes/Lysosomes using Super Paramagnetic Iron Oxide Nanoparticles
  - Suspension-adhesion assay
  - Mitochondrial metabolism
  - Confocal microscopy
  - Airyscan Imaging
  - Structured Illumination microscopy (SIM)
  - Transmission Electron microscopy (TEM)
- QUANTIFICATION AND STATISTICAL ANALYSIS
  - Statistics and reproducibility

SUPPLEMENTAL INFORMATION

Supplemental information can be found online at https://doi.org/10.1016/j.devcel.2024.03.030.

ACKNOWLEDGMENTS

This work was made possible through the financial support of VIB, KU Leuven (C14/21/095 and SMINF KA/20/085), the Research Foundation – Flanders (FWO; S006617N, G056017N, G078117N, G0C4220N, and I001322N), SAO-FRA (#2017/033 to M.B.; #2020/030 and 2022/022 to W.A.), and the Alzheimer Association (AARF-18-564825 to M.B., AARF-20-677499 to Z.-P.V.A., and AARF-23-1149740 to C.V.). T.L. and A.P. obtained a FWO doctoral fellowship (11K1124N and 1S35019N, respectively); C.V. is holder of a FWO postdoctoral mandate (12B7423N). The VIB BioImaging Core is acknowledged for providing access and support to confocal microscopy and EM. The authors wish to thank Max Gorelashvili, Yilmaz Niyaz, and Abel Pereira (Zeiss, Oberkochen) for access to the Zeiss Elyra-7 infrastructure at Oberkochen (Germany), Christine Michiels for generating Crispr-Cas9 APP KO cell lines, and David Demedts

for preparing DMSA-SPIONs. The graphical abstract was created with Biorender (https://www.biorender.com/).

AUTHOR CONTRIBUTIONS

M.B. designed, performed, and analyzed most experiments, prepared all manuscript figures, and participated in article writing and project conception. R.S. helped to set up and assisted with the DAPT and LICV experiments, as well as all experiments on primary neurons. A.E.-A. helped with live-imaging SIM, performed trajectory analysis, and assisted with LICVs experiments. E.-L.E. and I.V. carried out TEM imaging and quantification. Z.-P.V.A. quantified contact sites visualized by TEM. T.L. performed seahorse experiments and some LE/Lys Ca^{2+} storage experiments. C.V. and A.P. generated primary neuron cultures and performed their analysis with R.S., and K.W. did neuronal Ca^{2+} imaging. W.V. and S. V. K. helped with clone generation and biochemistry. B.P. created all codes for Image J quantification. C.V. and W.A. generated the graphical abstract. W.A. designed the overall research strategy, coordinated the experiments, and wrote the manuscript with feedback from the authors.

DECLARATION OF INTERESTS

The authors declare no competing interests.

Received: October 18, 2021
Revised: November 2, 2023
Accepted: March 20, 2024
Published: April 15, 2024

REFERENCES

1. Peric, A., and Annaert, W. (2015). Early etiology of Alzheimer's disease: tipping the balance toward autophagy or endosomal dysfunction? Acta Neuropathol. *129*, 363–381. https://doi.org/10.1007/s00401-014-1379-7.
2. Escamilla-Ayala, A.A., Sannerud, R., Mondin, M., Poersch, K., Vermeire, W., Paparelli, L., Berlage, C., Koenig, M., Chavez-Gutierrez, L., Ulbrich, M.H., et al. (2020). Super-resolution microscopy reveals majorly mono- and dimeric presenilin1/gamma-secretase at the cell surface. eLife *9*, e56679. https://doi.org/10.7554/eLife.56679.
3. Szaruga, M., Munteanu, B., Lismont, S., Veugelen, S., Horré, K., Mercken, M., Saido, T.C., Ryan, N.S., De Vos, T., Savvides, S.N., et al. (2017). Alzheimer's-Causing Mutations Shift Aβ Length by Destabilizing gamma-Secretase-Aβn Interactions. Cell *170*, 443–456.e14. https://doi.org/10.1016/j.cell.2017.07.004.
4. Shioi, J., Georgakopoulos, A., Mehta, P., Kouchi, Z., Litterst, C.M., Baki, L., and Robakis, N.K. (2007). FAD mutants unable to increase neurotoxic Abeta 42 suggest that mutation effects on neurodegeneration may be independent of effects on Abeta. J. Neurochem. *101*, 674–681. https://doi.org/10.1111/j.1471-4159.2006.04391.x.
5. De Strooper, B., and Karran, E. (2016). The Cellular Phase of Alzheimer's Disease. Cell *164*, 603–615. https://doi.org/10.1016/j.cell.2015.12.056.
6. Selkoe, D.J., and Hardy, J. (2016). The amyloid hypothesis of Alzheimer's disease at 25 years. EMBO Mol. Med. *8*, 595–608. https://doi.org/10.15252/emmm.201606210.
7. Boland, B., Kumar, A., Lee, S., Platt, F.M., Wegiel, J., Yu, W.H., and Nixon, R.A. (2008). Autophagy induction and autophagosome clearance in neurons: relationship to autophagic pathology in Alzheimer's disease. J. Neurosci. *28*, 6926–6937. https://doi.org/10.1523/JNEUROSCI.0800-08.2008.
8. Cataldo, A.M., Peterhoff, C.M., Troncoso, J.C., Gomez-Isla, T., Hyman, B.T., and Nixon, R.A. (2000). Endocytic pathway abnormalities precede amyloid beta deposition in sporadic Alzheimer's disease and Down syndrome: differential effects of APOE genotype and presenilin mutations. Am. J. Pathol. *157*, 277–286. https://doi.org/10.1016/s0002-9440(10)64538-5.
9. Cataldo, A.M., Petanceska, S., Peterhoff, C.M., Terio, N.B., Epstein, C.J., Villar, A., Carlson, E.J., Staufenbiel, M., and Nixon, R.A. (2003). App gene dosage modulates endosomal abnormalities of Alzheimer's disease in a segmental trisomy 16 mouse model of down syndrome. J. Neurosci. *23*, 6788–6792.
10. Takahashi, R.H., Almeida, C.G., Kearney, P.F., Yu, F., Lin, M.T., Milner, T.A., and Gouras, G.K. (2004). Oligomerization of Alzheimer's beta-amyloid within processes and synapses of cultured neurons and brain. J. Neurosci. *24*, 3592–3599. https://doi.org/10.1523/JNEUROSCI.5167-03.2004.
11. Small, S.A., Simoes-Spassov, S., Mayeux, R., and Petsko, G.A. (2017). Endosomal Traffic Jams Represent a Pathogenic Hub and Therapeutic Targettarget in Alzheimer's Disease. Trends Neurosci. *40*, 592–602. https://doi.org/10.1016/j.tins.2017.08.003.
12. Karch, C.M., and Goate, A.M. (2015). Alzheimer's disease risk genes and mechanisms of disease pathogenesis. Biol. Psychiatry *77*, 43–51. https://doi.org/10.1016/j.biopsych.2014.05.006.
13. Van Acker, Z.P., Bretou, M., and Annaert, W. (2019). Endo-lysosomal dysregulations and late-onset Alzheimer's disease: impact of genetic risk factors. Mol. Neurodegener. *14*, 20. https://doi.org/10.1186/s13024-019-0323-7.
14. Scheltens, P., De Strooper, B., Kivipelto, M., Holstege, H., Chételat, G., Teunissen, C.E., Cummings, J., and van der Flier, W.M. (2021). Alzheimer's disease. Lancet *397*, 1577–1590. https://doi.org/10.1016/S0140-6736(20)32205-4.
15. Gouras, G.K., Tampellini, D., Takahashi, R.H., and Capetillo-Zarate, E. (2010). Intraneuronal beta-amyloid accumulation and synapse pathology in Alzheimer's disease. Acta Neuropathol. *119*, 523–541. https://doi.org/10.1007/s00401-010-0679-9.
16. Woodruff, G., Reyna, S.M., Dunlap, M., Van Der Kant, R., Callender, J.A., Young, J.E., Roberts, E.A., and Goldstein, L.S. (2016). Defective Transcytosis of APP and Lipoproteins in Human iPSC-Derived Neurons with Familial Alzheimer's Disease Mutations. Cell Rep. *17*, 759–773. https://doi.org/10.1016/j.celrep.2016.09.034.
17. Kwart, D., Gregg, A., Scheckel, C., Murphy, E.A., Paquet, D., Duffield, M., Fak, J., Olsen, O., Darnell, R.B., and Tessier-Lavigne, M. (2019). A Large Panel of Isogenic APP and PSEN1 Mutant Human iPSC Neurons Reveals Shared Endosomal Abnormalities Mediated by APP beta-CTFs, Not Aβ. Neuron *104*, 256–270.e5. https://doi.org/10.1016/j.neuron.2019.07.010.
18. Hung, C.O.Y., and Livesey, F.J. (2018). Altered gamma-Secretase Processing of APP Disrupts Lysosome and Autophagosome Function in Monogenic Alzheimer's Disease. Cell Rep. *25*, 3647–3660.e2. https://doi.org/10.1016/j.celrep.2018.11.095.
19. Kim, S., Sato, Y., Mohan, P.S., Peterhoff, C., Pensalfini, A., Rigoglioso, A., Jiang, Y., and Nixon, R.A. (2016). Evidence that the rab5 effector APPL1 mediates APP-βCTF-induced dysfunction of endosomes in Down syndrome and Alzheimer's disease. Mol. Psychiatry *21*, 707–716. https://doi.org/10.1038/mp.2015.97.
20. Xu, W., Weissmiller, A.M., White, J.A., 2nd, Fang, F., Wang, X., Wu, Y., Pearn, M.L., Zhao, X., Sawa, M., Chen, S., et al. (2016). Amyloid precursor protein-mediated endocytic pathway disruption induces axonal dysfunction and neurodegeneration. J. Clin. Invest. *126*, 1815–1833. https://doi.org/10.1172/JCI82409.
21. Hung, C., Tuck, E., Stubbs, V., van der Lee, S.J., Aalfs, C., van Spaendonk, R., Scheltens, P., Hardy, J., Holstege, H., and Livesey, F.J. (2021). SORL1 deficiency in human excitatory neurons causes APP-dependent defects in the endolysosome-autophagy network. Cell Rep. *35*, 109259. https://doi.org/10.1016/j.celrep.2021.109259.
22. Lee, J.H., Yu, W.H., Kumar, A., Lee, S., Mohan, P.S., Peterhoff, C.M., Wolfe, D.M., Martinez-Vicente, M., Massey, A.C., Sovak, G., et al. (2010). Lysosomal proteolysis and autophagy require presenilin 1 and are disrupted by Alzheimer-related PS1 mutations. Cell *141*, 1146–1158. https://doi.org/10.1016/j.cell.2010.05.008.
23. Lee, J.H., McBrayer, M.K., Wolfe, D.M., Haslett, L.J., Kumar, A., Sato, Y., Lie, P.P., Mohan, P., Coffey, E.E., Kompella, U., et al. (2015). Presenilin 1

Maintains Lysosomal Ca(2+) Homeostasis via TRPML1 by Regulating vATPase-Mediated Lysosome Acidification. Cell Rep. *12*, 1430–1444. https://doi.org/10.1016/j.celrep.2015.07.050.

24. Coen, K., Flannagan, R.S., Baron, S., Carraro-Lacroix, L.R., Wang, D., Vermeire, W., Michiels, C., Munck, S., Baert, V., Sugita, S., et al. (2012). Lysosomal calcium homeostasis defects, not proton pump defects, cause endo-lysosomal dysfunction in PSEN-deficient cells. J. Cell Biol. *198*, 23–35. https://doi.org/10.1083/jcb.201201076.
25. Neely, K.M., Green, K.N., and LaFerla, F.M. (2011). Presenilin is necessary for efficient proteolysis through the autophagy-lysosome system in a gamma-secretase-independent manner. J. Neurosci. *31*, 2781–2791. https://doi.org/10.1523/JNEUROSCI.5156-10.2010.
26. Zhang, X., Garbett, K., Veeraraghavalu, K., Wilburn, B., Gilmore, R., Mirnics, K., and Sisodia, S.S. (2012). A role for presenilins in autophagy revisited: normal acidification of lysosomes in cells lacking PSEN1 and PSEN2. J. Neurosci. *32*, 8633–8648. https://doi.org/10.1523/JNEUROSCI.0556-12.2012.
27. Reddy, K., Cusack, C.L., Nnah, I.C., Khayati, K., Saqcena, C., Huynh, T.B., Noggle, S.A., Ballabio, A., and Dobrowolski, R. (2016). Dysregulation of Nutrient Sensing and CLEARance in Presenilin Deficiency. Cell Rep. *14*, 2166–2179. https://doi.org/10.1016/j.celrep.2016.02.006.
28. Im, E., Jiang, Y., Stavrides, P.H., Darji, S., Erdjument-Bromage, H., Neubert, T.A., Choi, J.Y., Wegiel, J., Lee, J.H., and Nixon, R.A. (2023). Lysosomal dysfunction in Down syndrome and Alzheimer mouse models is caused by v-ATPase inhibition by Tyr(682)-phosphorylated APP βCTF. Sci. Adv. *9*, eadg1925. https://doi.org/10.1126/sciadv.adg1925.
29. Jadot, M., Colmant, C., Wattiaux-De Coninck, S., and Wattiaux, R. (1984). Intralysosomal hydrolysis of glycyl-L-phenylalanine 2-naphthylamide. Biochem. J. *219*, 965–970. https://doi.org/10.1042/bj2190965.
30. Morgan, A.J., Yuan, Y., Patel, S., and Galione, A. (2020). Does lysosomal rupture evoke Ca^{2+} release? A question of pores and stores. Cell Calcium *86*, 102139. https://doi.org/10.1016/j.ceca.2019.102139.
31. Yuan, Y., Kilpatrick, B.S., Gerndt, S., Bracher, F., Grimm, C., Schapira, A.H., and Patel, S. (2021). The lysosomotrope GPN mobilises Ca^{2+} from acidic organelles. J. Cell Sci. *134*, jcs256578. https://doi.org/10.1242/jcs.256578.
32. Esselens, C., Oorschot, V., Baert, V., Raemaekers, T., Spittaels, K., Serneels, L., Zheng, H., Saftig, P., De Strooper, B., Klumperman, J., and Annaert, W. (2004). Presenilin 1 mediates the turnover of telencephalin in hippocampal neurons via an autophagic degradative pathway. J. Cell Biol. *166*, 1041–1054. https://doi.org/10.1083/jcb.200406060.
33. Annaert, W.G., Esselens, C., Baert, V., Boeve, C., Snellings, G., Cupers, P., Craessaerts, K., and De Strooper, B. (2001). Interaction with telencephalin and the amyloid precursor protein predicts a ring structure for presenilins. Neuron *32*, 579–589. https://doi.org/10.1016/s0896-6273(01)00512-8.
34. Mindell, J.A. (2012). Lysosomal acidification mechanisms. Annu. Rev. Physiol. *74*, 69–86. https://doi.org/10.1146/annurev-physiol-012110-142317.
35. Chin, M.Y., Patwardhan, A.R., Ang, K.H., Wang, A.L., Alquezar, C., Welch, M., Nguyen, P.T., Grabe, M., Molofsky, A.V., Arkin, M.R., and Kao, A.W. (2021). Genetically Encoded, pH-Sensitive mTFP1 Biosensor for Probing Lysosomal pH. ACS Sens. *6*, 2168–2180. https://doi.org/10.1021/acssensors.0c02318.
36. Maxson, M.E., Abbas, Y.M., Wu, J.Z., Plumb, J.D., Grinstein, S., and Rubinstein, J.L. (2022). Detection and quantification of the vacuolar H+ATPase using the Legionella effector protein SidK. J. Cell Biol. *221*, e202107174. https://doi.org/10.1083/jcb.202107174.
37. Huotari, J., and Helenius, A. (2011). Endosome maturation. EMBO J. *30*, 3481–3500. https://doi.org/10.1038/emboj.2011.286.
38. Kessissoglou, I.A., Langui, D., Hasan, A., Maral, M., Dutta, S.B., Hiesinger, P.R., and Hassan, B.A. (2020). The Drosophila amyloid precursor protein homologue mediates neuronal survival and neuroglial interactions. PLoS Biol. *18*, e3000703. https://doi.org/10.1371/journal.pbio.3000703.
39. Balasubramanian, N., Scott, D.W., Castle, J.D., Casanova, J.E., and Schwartz, M.A. (2007). Arf6 and microtubules in adhesion-dependent trafficking of lipid rafts. Nat. Cell Biol. *9*, 1381–1391. https://doi.org/10.1038/ncb1657.
40. Treusch, S., Hamamichi, S., Goodman, J.L., Matlack, K.E., Chung, C.Y., Baru, V., Shulman, J.M., Parrado, A., Bevis, B.J., Valastyan, J.S., et al. (2011). Functional links between Abeta toxicity, endocytic trafficking, and Alzheimer's disease risk factors in yeast. Science *334*, 1241–1245. https://doi.org/10.1126/science.1213210.
41. Kopan, R., and Ilagan, M.X. (2004). Gamma-secretase: proteasome of the membrane? Nat. Rev. Mol. Cell Biol. *5*, 499–504. https://doi.org/10.1038/nrm1406.
42. Deyts, C., Vetrivel, K.S., Das, S., Shepherd, Y.M., Dupré, D.J., Thinakaran, G., and Parent, A.T. (2012). Novel GαS-protein signaling associated with membrane-tethered amyloid precursor protein intracellular domain. J. Neurosci. *32*, 1714–1729. https://doi.org/10.1523/JNEUROSCI.5433-11.2012.
43. Deyts, C., Clutter, M., Pierce, N., Chakrabarty, P., Ladd, T.B., Goddi, A., Rosario, A.M., Cruz, P., Vetrivel, K., Wagner, S.L., et al. (2019). APP-Mediated Signaling Prevents Memory Decline in Alzheimer's Disease Mouse Model. Cell Rep. *27*, 1345–1355.e6. https://doi.org/10.1016/j.celrep.2019.03.087.
44. Andersen, O.M., Reiche, J., Schmidt, V., Gotthardt, M., Spoelgen, R., Behlke, J., von Arnim, C.A., Breiderhoff, T., Jansen, P., Wu, X., et al. (2005). Neuronal sorting protein-related receptor sorLA/LR11 regulates processing of the amyloid precursor protein. Proc. Natl. Acad. Sci. USA *102*, 13461–13466. https://doi.org/10.1073/pnas.0503689102.
45. Borg, J.P., Ooi, J., Levy, E., and Margolis, B. (1996). The phosphotyrosine interaction domains of X11 and FE65 bind to distinct sites on the YENPTY motif of amyloid precursor protein. Mol. Cell. Biol. *16*, 6229–6241. https://doi.org/10.1128/mcb.16.11.6229.
46. Howell, B.W., Lanier, L.M., Frank, R., Gertler, F.B., and Cooper, J.A. (1999). The disabled 1 phosphotyrosine-binding domain binds to the internalization signals of transmembrane glycoproteins and to phospholipids. Mol. Cell. Biol. *19*, 5179–5188. https://doi.org/10.1128/mcb.19.7.5179.
47. Currinn, H., Guscott, B., Balklava, Z., Rothnie, A., and Wassmer, T. (2016). APP controls the formation of PI(3,5)P(2) vesicles through its binding of the PIKfyve complex. Cell. Mol. Life Sci. *73*, 393–408. https://doi.org/10.1007/s00018-015-1993-0.
48. Ikonomov, O.C., Sbrissa, D., Foti, M., Carpentier, J.L., and Shisheva, A. (2003). PIKfyve controls fluid phase endocytosis but not recycling/degradation of endocytosed receptors or sorting of procathepsin D by regulating multivesicular body morphogenesis. Mol. Biol. Cell *14*, 4581–4591. https://doi.org/10.1091/mbc.e03-04-0222.
49. Netzer, W.J., Dou, F., Cai, D., Veach, D., Jean, S., Li, Y., Bornmann, W.G., Clarkson, B., Xu, H., and Greengard, P. (2003). Gleevec inhibits beta-amyloid production but not Notch cleavage. Proc. Natl. Acad. Sci. USA *100*, 12444–12449. https://doi.org/10.1073/pnas.1534745100.
50. Shen, D., Wang, X., Li, X., Zhang, X., Yao, Z., Dibble, S., Dong, X.P., Yu, T., Lieberman, A.P., Showalter, H.D., and Xu, H. (2012). Lipid storage disorders block lysosomal trafficking by inhibiting a TRP channel and lysosomal calcium release. Nat. Commun. *3*, 731. https://doi.org/10.1038/ncomms1735.
51. Garrity, A.G., Wang, W., Collier, C.M., Levey, S.A., Gao, Q., and Xu, H. (2016). The endoplasmic reticulum, not the pH gradient, drives calcium refilling of lysosomes. eLife *5*, e15887. https://doi.org/10.7554/eLife.15887.
52. Yang, J., Zhao, Z., Gu, M., Feng, X., and Xu, H. (2019). Release and uptake mechanisms of vesicular Ca^{2+} stores. Protein Cell *10*, 8–19. https://doi.org/10.1007/s13238-018-0523-x.

53. Burgoyne, T., Patel, S., and Eden, E.R. (2015). Calcium signaling at ER membrane contact sites. Biochim. Biophys. Acta *1853*, 2012–2017. https://doi.org/10.1016/j.bbamcr.2015.01.022.

54. Alpy, F., Rousseau, A., Schwab, Y., Legueux, F., Stoll, I., Wendling, C., Spiegelhalter, C., Kessler, P., Mathelin, C., Rio, M.C., et al. (2013). STARD3 or STARD3NL and VAP form a novel molecular tether between late endosomes and the ER. J. Cell Sci. *126*, 5500–5512. https://doi.org/10.1242/jcs.139295.

55. King, C., SenGupta, P., Seo, A.Y., and Lippincott-Schwartz, J. (2020). ER membranes exhibit phase behavior at sites of organelle contact. Proc. Natl. Acad. Sci. USA *117*, 7225–7235. https://doi.org/10.1073/pnas.1910854117.

56. Montesinos, J., Pera, M., Larrea, D., Guardia-Laguarta, C., Agrawal, R.R., Velasco, K.R., Yun, T.D., Stavrovskaya, I.G., Xu, Y., Koo, S.Y., et al. (2020). The Alzheimer's disease-associated C99 fragment of APP regulates cellular cholesterol trafficking. EMBO J. *39*, e103791. https://doi.org/10.15252/embj.2019103791.

57. Pera, M., Larrea, D., Guardia-Laguarta, C., Montesinos, J., Velasco, K.R., Agrawal, R.R., Xu, Y., Chan, R.B., Di Paolo, G., Mehler, M.F., et al. (2017). Increased localization of APP-C99 in mitochondria-associated ER membranes causes mitochondrial dysfunction in Alzheimer disease. EMBO J. *36*, 3356–3371. https://doi.org/10.15252/embj.201796797.

58. Giordano, F., Saheki, Y., Idevall-Hagren, O., Colombo, S.F., Pirruccello, M., Milosevic, I., Gracheva, E.O., Bagriantsev, S.N., Borgese, N., and De Camilli, P. (2013). PI(4,5)P(2)-dependent and Ca(2+)-regulated ER-PM interactions mediated by the extended synaptotagmins. Cell *153*, 1494–1509. https://doi.org/10.1016/j.cell.2013.05.026.

59. Wu, Y., Huang, P., and Dong, X.P. (2021). Lysosomal Calcium Channels in Autophagy and Cancer. Cancers (Basel) *13*, 1299. https://doi.org/10.3390/cancers13061299.

60. Lloyd-Evans, E., Morgan, A.J., He, X., Smith, D.A., Elliot-Smith, E., Sillence, D.J., Churchill, G.C., Schuchman, E.H., Galione, A., and Platt, F.M. (2008). Niemann-Pick disease type C1 is a sphingosine storage disease that causes deregulation of lysosomal calcium. Nat. Med. *14*, 1247–1255. https://doi.org/10.1038/nm.1876.

61. Davis, O.B., Shin, H.R., Lim, C.Y., Wu, E.Y., Kukurugya, M., Maher, C.F., Perera, R.M., Ordonez, M.P., and Zoncu, R. (2021). NPC1-mTORC1 Signaling Couples Cholesterol Sensing to Organelle Homeostasis and Is a Targetable Pathway in Niemann-Pick Type C. Dev. Cell *56*, 260–276.e7. https://doi.org/10.1016/j.devcel.2020.11.016.

62. Lim, C.Y., Davis, O.B., Shin, H.R., Zhang, J., Berdan, C.A., Jiang, X., Counihan, J.L., Ory, D.S., Nomura, D.K., and Zoncu, R. (2019). ER-lysosome contacts enable cholesterol sensing by mTORC1 and drive aberrant growth signalling in Niemann-Pick type C. Nat. Cell Biol. *21*, 1206–1218. https://doi.org/10.1038/s41556-019-0391-5.

63. Burgett, A.W., Poulsen, T.B., Wangkanont, K., Anderson, D.R., Kikuchi, C., Shimada, K., Okubo, S., Fortner, K.C., Mimaki, Y., Kuroda, M., et al. (2011). Natural products reveal cancer cell dependence on oxysterol-binding proteins. Nat. Chem. Biol. *7*, 639–647. https://doi.org/10.1038/nchembio.625.

64. Hoque, S., Kondo, Y., Sakata, N., Yamada, Y., Fukaura, M., Higashi, T., Motoyama, K., Arima, H., Higaki, K., Hayashi, A., et al. (2020). Differential Effects of 2-Hydroxypropyl-Cyclodextrins on Lipid Accumulation in Npc1-Null Cells. Int. J. Mol. Sci. *21*, 898. https://doi.org/10.3390/ijms21030898.

65. Singhal, A., Krystofiak, E.S., Jerome, W.G., and Song, B. (2020). 2-Hydroxypropyl-gamma-cyclodextrin overcomes NPC1 deficiency by enhancing lysosome-ER association and autophagy. Sci. Rep. *10*, 8663. https://doi.org/10.1038/s41598-020-65627-4.

66. Zhang, M., Haapasalo, A., Kim, D.Y., Ingano, L.A., Pettingell, W.H., and Kovacs, D.M. (2006). Presenilin/gamma-secretase activity regulates protein clearance from the endocytic recycling compartment. FASEB J. *20*, 1176–1178. https://doi.org/10.1096/fj.05-5531fje.

67. Bucci, C., Parton, R.G., Mather, I.H., Stunnenberg, H., Simons, K., Hoflack, B., and Zerial, M. (1992). The small GTPase rab5 functions as a regulatory factor in the early endocytic pathway. Cell *70*, 715–728. https://doi.org/10.1016/0092-8674(92)90306-w.

68. Grbovic, O.M., Mathews, P.M., Jiang, Y., Schmidt, S.D., Dinakar, R., Summers-Terio, N.B., Ceresa, B.P., Nixon, R.A., and Cataldo, A.M. (2003). Rab5-stimulated up-regulation of the endocytic pathway increases intracellular beta-cleaved amyloid precursor protein carboxyl-terminal fragment levels and Abeta production. J. Biol. Chem. *278*, 31261–31268. https://doi.org/10.1074/jbc.M304122200.

69. Rojas, R., van Vlijmen, T., Mardones, G.A., Prabhu, Y., Rojas, A.L., Mohammed, S., Heck, A.J., Raposo, G., van der Sluijs, P., and Bonifacino, J.S. (2008). Regulation of retromer recruitment to endosomes by sequential action of Rab5 and Rab7. J. Cell Biol. *183*, 513–526. https://doi.org/10.1083/jcb.200804048.

70. Pensalfini, A., Kim, S., Subbanna, S., Bleiwas, C., Goulbourne, C.N., Stavrides, P.H., Jiang, Y., Lee, J.H., Darji, S., Pawlik, M., et al. (2020). Endosomal Dysfunction Induced by Directly Overactivating Rab5 Recapitulates Prodromal and Neurodegenerative Features of Alzheimer's Disease. Cell Rep. *33*, 108420. https://doi.org/10.1016/j.celrep.2020.108420.

71. Small, S.A., Kent, K., Pierce, A., Leung, C., Kang, M.S., Okada, H., Honig, L., Vonsattel, J.P., and Kim, T.W. (2005). Model-guided microarray implicates the retromer complex in Alzheimer's disease. Ann. Neurol. *58*, 909–919. https://doi.org/10.1002/ana.20667.

72. Marquer, C., Tian, H., Yi, J., Bastien, J., Dall'Armi, C., Yang-Klingler, Y., Zhou, B., Chan, R.B., and Di Paolo, G. (2016). Arf6 controls retromer traffic and intracellular cholesterol distribution via a phosphoinositide-based mechanism. Nat. Commun. *7*, 11919. https://doi.org/10.1038/ncomms11919.

73. Thimiri Govinda Raj, D.B., Ghesquière, B., Tharkeshwar, A.K., Coen, K., Derua, R., Vanderschaeghe, D., Rysman, E., Bagadi, M., Baatsen, P., De Strooper, B., et al. (2011). A novel strategy for the comprehensive analysis of the biomolecular composition of isolated plasma membranes. Mol. Syst. Biol. *7*, 541. https://doi.org/10.1038/msb.2011.74.

74. Small, S.A., and Petsko, G.A. (2020). Endosomal recycling reconciles the Alzheimer's disease paradox. Sci. Transl. Med. *12*, eabb1717. https://doi.org/10.1126/scitranslmed.abb1717.

75. Marambaud, P., Wen, P.H., Dutt, A., Shioi, J., Takashima, A., Siman, R., and Robakis, N.K. (2003). A CBP binding transcriptional repressor produced by the PS1/epsilon-cleavage of N-cadherin is inhibited by PS1 FAD mutations. Cell *114*, 635–645. https://doi.org/10.1016/j.cell.2003.08.008.

76. Sardi, S.P., Murtie, J., Koirala, S., Patten, B.A., and Corfas, G. (2006). Presenilin-dependent ErbB4 nuclear signaling regulates the timing of astrogenesis in the developing brain. Cell *127*, 185–197. https://doi.org/10.1016/j.cell.2006.07.037.

77. Jurisch-Yaksi, N., Sannerud, R., and Annaert, W. (2013). A fast growing spectrum of biological functions of gamma-secretase in development and disease. Biochim. Biophys. Acta *1828*, 2815–2827. https://doi.org/10.1016/j.bbamem.2013.04.016.

78. Bray, S.J. (2016). Notch signalling in context. Nat. Rev. Mol. Cell Biol. *17*, 722–735. https://doi.org/10.1038/nrm.2016.94.

79. Jäger, S., Leuchtenberger, S., Martin, A., Czirr, E., Wesselowski, J., Dieckmann, M., Waldron, E., Korth, C., Koo, E.H., Heneka, M., et al. (2009). alpha-secretase mediated conversion of the amyloid precursor protein derived membrane stub C99 to C83 limits Abeta generation. J. Neurochem. *111*, 1369–1382. https://doi.org/10.1111/j.1471-4159.2009.06420.x.

80. Cao, X., and Südhof, T.C. (2001). A transcriptionally [correction of transcriptively] active complex of APP with Fe65 and histone acetyltransferase Tip60. Science *293*, 115–120. https://doi.org/10.1126/science.1058783.

81. Müller, T., Concannon, C.G., Ward, M.W., Walsh, C.M., Tirniceriu, A.L., Tribl, F., Kögel, D., Prehn, J.H., and Egensperger, R. (2007). Modulation of gene expression and cytoskeletal dynamics by the

amyloid precursor protein intracellular domain (AICD). Mol. Biol. Cell *18*, 201–210. https://doi.org/10.1091/mbc.e06-04-0283.

82. Pardossi-Piquard, R., Petit, A., Kawarai, T., Sunyach, C., Alves da Costa, C., Vincent, B., Ring, S., D'Adamio, L., Shen, J., Müller, U., et al. (2005). Presenilin-dependent transcriptional control of the Abeta-degrading enzyme neprilysin by intracellular domains of betaAPP and APLP. Neuron *46*, 541–554. https://doi.org/10.1016/j.neuron.2005.04.008.
83. Alves da Costa, C., Sunyach, C., Pardossi-Piquard, R., Sévalle, J., Vincent, B., Boyer, N., Kawarai, T., Girardot, N., St George-Hyslop, P., and Checler, F. (2006). Presenilin-dependent gamma-secretase-mediated control of p53-associated cell death in Alzheimer's disease. J. Neurosci. *26*, 6377–6385. https://doi.org/10.1523/JNEUROSCI.0651-06.2006.
84. Kimberly, W.T., Zheng, J.B., Guénette, S.Y., and Selkoe, D.J. (2001). The intracellular domain of the beta-amyloid precursor protein is stabilized by Fe65 and translocates to the nucleus in a notch-like manner. J. Biol. Chem. *276*, 40288–40292. https://doi.org/10.1074/jbc.C100447200.
85. Leyssen, M., Ayaz, D., Hébert, S.S., Reeve, S., De Strooper, B., and Hassan, B.A. (2005). Amyloid precursor protein promotes post-developmental neurite arborization in the Drosophila brain. EMBO J. *24*, 2944–2955. https://doi.org/10.1038/sj.emboj.7600757.
86. Deyts, C., Clutter, M., Herrera, S., Jovanovic, N., Goddi, A., and Parent, A.T. (2016). Loss of presenilin function is associated with a selective gain of APP function. eLife *5*, e15645. https://doi.org/10.7554/eLife.15645.
87. Cao, X., and Südhof, T.C. (2004). Dissection of amyloid-beta precursor protein-dependent transcriptional transactivation. J. Biol. Chem. *279*, 24601–24611. https://doi.org/10.1074/jbc.M402248200.
88. Hass, M.R., and Yankner, B.A. (2005). A {gamma}-secretase-independent mechanism of signal transduction by the amyloid precursor protein. J. Biol. Chem. *280*, 36895–36904. https://doi.org/10.1074/jbc.M502861200.
89. Del Prete, D., Suski, J.M., Oulès, B., Debayle, D., Gay, A.S., Lacas-Gervais, S., Bussiere, R., Bauer, C., Pinton, P., Paterlini-Bréchot, P., et al. (2017). Localization and Processing of the Amyloid-beta Protein Precursor in Mitochondria-Associated Membranes. J. Alzheimers Dis. *55*, 1549–1570. https://doi.org/10.3233/JAD-160953.
90. Bhattacharyya, R., Black, S.E., Lotlikar, M.S., Fenn, R.H., Jorfi, M., Kovacs, D.M., and Tanzi, R.E. (2021). Axonal generation of amyloid-beta from palmitoylated APP in mitochondria-associated endoplasmic reticulum membranes. Cell Rep. *35*, 109134. https://doi.org/10.1016/j.celrep.2021.109134.
91. Lee, S.E., Kwon, D., Shin, N., Kong, D., Kim, N.G., Kim, H.Y., Kim, M.J., Choi, S.W., and Kang, K.S. (2022). Accumulation of APP-CTF induces mitophagy dysfunction in the iNSCs model of Alzheimer's disease. Cell Death Discov. *8*, 1. https://doi.org/10.1038/s41420-021-00796-3.
92. Wouters, R., Michiels, C., Sannerud, R., Kleizen, B., Dillen, K., Vermeire, W., Ayala, A.E., Demedts, D., Schekman, R., and Annaert, W. (2021). Assembly of gamma-secretase occurs through stable dimers after exit from the endoplasmic reticulum. J. Cell Biol. *220*. https://doi.org/10.1083/jcb.201911104.
93. Marchetti, P., Fovez, Q., Germain, N., Khamari, R., and Kluza, J. (2020). Mitochondrial spare respiratory capacity: Mechanisms, regulation, and significance in non-transformed and cancer cells. FASEB J. *34*, 13106–13124. https://doi.org/10.1096/fj.202000767R.
94. Sarasija, S., Laboy, J.T., Ashkavand, Z., Bonner, J., Tang, Y., and Norman, K.R. (2018). Presenilin mutations deregulate mitochondrial Ca^{2+} homeostasis and metabolic activity causing neurodegeneration in Caenorhabditis elegans. eLife *7*, e33052. https://doi.org/10.7554/eLife.33052.
95. Kipanyula, M.J., Contreras, L., Zampese, E., Lazzari, C., Wong, A.K., Pizzo, P., Fasolato, C., and Pozzan, T. (2012). Ca2+ dysregulation in neurons from transgenic mice expressing mutant presenilin 2. Aging Cell *11*, 885–893. https://doi.org/10.1111/j.1474-9726.2012.00858.x.
96. Zampese, E., Fasolato, C., Pozzan, T., and Pizzo, P. (2011). Presenilin-2 modulation of ER-mitochondria interactions: FAD mutations, mechanisms and pathological consequences. Commun. Integr. Biol. *4*, 357–360. https://doi.org/10.4161/cib.4.3.15160.
97. Contino, S., Porporato, P.E., Bird, M., Marinangeli, C., Opsomer, R., Sonveaux, P., Bontemps, F., Dewachter, I., Octave, J.N., Bertrand, L., et al. (2017). Presenilin 2-Dependent Maintenance of Mitochondrial Oxidative Capacity and Morphology. Front. Physiol. *8*, 796. https://doi.org/10.3389/fphys.2017.00796.
98. Calvo-Rodriguez, M., and Bacskai, B.J. (2021). Mitochondria and Calcium in Alzheimer's Disease: From Cell Signaling to Neuronal Cell Death. Trends Neurosci. *44*, 136–151. https://doi.org/10.1016/j.tins.2020.10.004.
99. Callens, M., Kraskovskaya, N., Derevtsova, K., Annaert, W., Bultynck, G., Bezprozvanny, I., and Vervliet, T. (2021). The role of Bcl-2 proteins in modulating neuronal Ca^{2+} signaling in health and in Alzheimer's disease. Biochim. Biophys. Acta Mol. Cell Res. *1868*, 118997. https://doi.org/10.1016/j.bbamcr.2021.118997.
100. Vaillant-Beuchot, L., Mary, A., Pardossi-Piquard, R., Bourgeois, A., Lauritzen, I., Eysert, F., Kinoshita, P.F., Cazareth, J., Badot, C., Fragaki, K., et al. (2021). Accumulation of amyloid precursor protein C-terminal fragments triggers mitochondrial structure, function, and mitophagy defects in Alzheimer's disease models and human brains. Acta Neuropathol. *141*, 39–65. https://doi.org/10.1007/s00401-020-02234-7.
101. Wong, Y.C., Ysselstein, D., and Krainc, D. (2018). Mitochondria-lysosome contacts regulate mitochondrial fission via RAB7 GTP hydrolysis. Nature *554*, 382–386. https://doi.org/10.1038/nature25486.
102. van Veen, S., Martin, S., Van den Haute, C., Benoy, V., Lyons, J., Vanhoutte, R., Kahler, J.P., Decuypere, J.P., Gelders, G., Lambie, E., et al. (2020). ATP13A2 deficiency disrupts lysosomal polyamine export. Nature *578*, 419–424. https://doi.org/10.1038/s41586-020-1968-7.
103. Plotegher, N., and Duchen, M.R. (2017). Mitochondrial Dysfunction and Neurodegeneration in Lysosomal Storage Disorders. Trends Mol. Med. *23*, 116–134. https://doi.org/10.1016/j.molmed.2016.12.003.
104. Van Acker, Z.P., Perdok, A., Hellemans, R., North, K., Vorsters, I., Cappel, C., Dehairs, J., Swinnen, J.V., Sannerud, R., Bretou, M., et al. (2023). Phospholipase D3 degrades mitochondrial DNA to regulate nucleotide signaling and APP metabolism. Nat. Commun. *14*, 2847. https://doi.org/10.1038/s41467-023-38501-w.
105. Couttas, T.A., Kain, N., Daniels, B., Lim, X.Y., Shepherd, C., Kril, J., Pickford, R., Li, H., Garner, B., and Don, A.S. (2014). Loss of the neuroprotective factor Sphingosine 1-phosphate early in Alzheimer's disease pathogenesis. Acta Neuropathol. Commun. *2*, 9. https://doi.org/10.1186/2051-5960-2-9.
106. van der Kant, R., and Neefjes, J. (2014). Small regulators, major consequences – Ca^{2+} and cholesterol at the endosome-ER interface. J. Cell Sci. *127*, 929–938. https://doi.org/10.1242/jcs.137539.
107. Roney, J.C., Li, S., Farfel-Becker, T., Huang, N., Sun, T., Xie, Y., Cheng, X.T., Lin, M.Y., Platt, F.M., and Sheng, Z.H. (2021). Lipid-mediated motor-adaptor sequestration impairs axonal lysosome delivery leading to autophagic stress and dystrophy in Niemann-Pick type C. Dev. Cell *56*, 1452–1468.e8. https://doi.org/10.1016/j.devcel.2021.03.032.
108. Lebrand, C., Corti, M., Goodson, H., Cosson, P., Cavalli, V., Mayran, N., Fauré, J., and Gruenberg, J. (2002). Late endosome motility depends on lipids via the small GTPase Rab7. EMBO J. *21*, 1289–1300. https://doi.org/10.1093/emboj/21.6.1289.
109. Essayan-Perez, S., and Südhof, T.C. (2023). Neuronal gamma-secretase regulates lipid metabolism, linking cholesterol to synaptic dysfunction in Alzheimer's disease. Neuron *111*, 3176–3194.e7. https://doi.org/10.1016/j.neuron.2023.07.005.
110. Lie, P.P.Y., Yoo, L., Goulbourne, C.N., Berg, M.J., Stavrides, P., Huo, C., Lee, J.H., and Nixon, R.A. (2022). Axonal transport of late endosomes and amphisomes is selectively modulated by local Ca^{2+} efflux and disrupted by PSEN1 loss of function. Sci. Adv. *8*, eabj5716. https://doi.org/10.1126/sciadv.abj5716.

111. Atakpa, P., Thillaiappan, N.B., Mataragka, S., Prole, D.L., and Taylor, C.W. (2018). IP(3) Receptors Preferentially Associate with ER-Lysosome Contact Sites and Selectively Deliver Ca^{2+} to Lysosomes. Cell Rep. *25*, 3180–3193.e7. https://doi.org/10.1016/j.celrep.2018.11.064.

112. Pera, M., Alcolea, D., Sánchez-Valle, R., Guardia-Laguarta, C., Colom-Cadena, M., Badiola, N., Suárez-Calvet, M., Lladó, A., Barrera-Ocampo, A.A., Sepulveda-Falla, D., et al. (2013). Distinct patterns of APP processing in the CNS in autosomal-dominant and sporadic Alzheimer disease. Acta Neuropathol. *125*, 201–213. https://doi.org/10.1007/s00401-012-1062-9.

113. Pulina, M.V., Hopkins, M., Haroutunian, V., Greengard, P., and Bustos, V. (2020). C99 selectively accumulates in vulnerable neurons in Alzheimer's disease. Alzheimers Dement. *16*, 273–282. https://doi.org/10.1016/j.jalz.2019.09.002.

114. De Strooper, B. (2014). Lessons from a failed gamma-secretase Alzheimer trial. Cell *159*, 721–726. https://doi.org/10.1016/j.cell.2014.10.016.

115. Checler, F., Afram, E., Pardossi-Piquard, R., and Lauritzen, I. (2021). Is gamma-secretase a beneficial inactivating enzyme of the toxic APP C-terminal fragment C99? J. Biol. Chem. *296*, 100489. https://doi.org/10.1016/j.jbc.2021.100489.

116. Janssens, J., Hermans, B., Vandermeeren, M., Barale-Thomas, E., Borgers, M., Willems, R., Meulders, G., Wintmolders, C., Van den Bulck, D., Bottelbergs, A., et al. (2021). Passive immunotherapy with a novel antibody against 3pE-modified Abeta demonstrates potential for enhanced efficacy and favorable safety in combination with BACE inhibitor treatment in plaque-depositing mice. Neurobiol. Dis. *154*, 105365. https://doi.org/10.1016/j.nbd.2021.105365.

117. Herreman, A., Hartmann, D., Annaert, W., Saftig, P., Craessaerts, K., Serneels, L., Umans, L., Schrijvers, V., Checler, F., Vanderstichele, H., et al. (1999). Presenilin 2 deficiency causes a mild pulmonary phenotype and no changes in amyloid precursor protein processing but enhances the embryonic lethal phenotype of presenilin 1 deficiency. Proc. Natl. Acad. Sci. USA *96*, 11872–11877. https://doi.org/10.1073/pnas.96.21.11872.

118. Tharkeshwar, A.K., Trekker, J., Vermeire, W., Pauwels, J., Sannerud, R., Priestman, D.A., Te Vruchte, D., Vints, K., Baatsen, P., Decuypere, J.P., et al. (2017). A novel approach to analyze lysosomal dysfunctions through subcellular proteomics and lipidomics: the case of NPC1 deficiency. Sci. Rep. *7*, 41408. https://doi.org/10.1038/srep41408.

119. De Strooper, B., Saftig, P., Craessaerts, K., Vanderstichele, H., Guhde, G., Annaert, W., Von Figura, K., and Van Leuven, F. (1998). Deficiency of presenilin-1 inhibits the normal cleavage of amyloid precursor protein. Nature *391*, 387–390. https://doi.org/10.1038/34910.

120. Ma, W., and Mayr, C. (2018). A Membraneless Organelle Associated with the Endoplasmic Reticulum Enables 3′UTR-Mediated Protein-Protein Interactions. Cell *175*, 1492–1506.e19. https://doi.org/10.1016/j.cell.2018.10.007.

121. Shibata, Y., Voss, C., Rist, J.M., Hu, J., Rapoport, T.A., Prinz, W.A., and Voeltz, G.K. (2008). The reticulon and DP1/Yop1p proteins form immobile oligomers in the tubular endoplasmic reticulum. J. Biol. Chem. *283*, 18892–18904. https://doi.org/10.1074/jbc.M800986200.

122. Zewe, J.P., Wills, R.C., Sangappa, S., Goulden, B.D., and Hammond, G.R. (2018). SAC1 degrades its lipid substrate PtdIns4P in the endoplasmic reticulum to maintain a steep chemical gradient with donor membranes. eLife *7*, e35588. https://doi.org/10.7554/eLife.35588.

123. Schindelin, J., Arganda-Carreras, I., Frise, E., Kaynig, V., Longair, M., Pietzsch, T., Preibisch, S., Rueden, C., Saalfeld, S., Schmid, B., et al. (2012). Fiji: an open-source platform for biological-image analysis. Nat. Methods *9*, 676–682. https://doi.org/10.1038/nmeth.2019.

124. Raemaekers, T., Peric, A., Baatsen, P., Sannerud, R., Declerck, I., Baert, V., Michiels, C., and Annaert, W. (2012). ARF6-mediated endosomal transport of Telencephalin affects dendritic filopodia-to-spine maturation. EMBO J. *31*, 3252–3269. https://doi.org/10.1038/emboj.2012.182.

125. Spasic, D., Raemaekers, T., Dillen, K., Declerck, I., Baert, V., Serneels, L., Füllekrug, J., and Annaert, W. (2007). Rer1p competes with APH-1 for binding to nicastrin and regulates gamma-secretase complex assembly in the early secretory pathway. J. Cell Biol. *176*, 629–640. https://doi.org/10.1083/jcb.200609180.

126. Spasic, D., Tolia, A., Dillen, K., Baert, V., De Strooper, B., Vrijens, S., and Annaert, W. (2006). Presenilin-1 maintains a nine-transmembrane topology throughout the secretory pathway. J. Biol. Chem. *281*, 26569–26577. https://doi.org/10.1074/jbc.M600592200.

127. Annaert, W.G., Levesque, L., Craessaerts, K., Dierinck, I., Snellings, G., Westaway, D., George-Hyslop, P.S., Cordell, B., Fraser, P., and De Strooper, B. (1999). Presenilin 1 controls gamma-secretase processing of amyloid precursor protein in pre-golgi compartments of hippocampal neurons. J. Cell Biol. *147*, 277–294. https://doi.org/10.1083/jcb.147.2.277.

128. Di Mattia, T., Martinet, A., Ikhlef, S., McEwen, A.G., Nominé, Y., Wendling, C., Poussin-Courmontagne, P., Voilquin, L., Eberling, P., Ruffenach, F., et al. (2020). FFAT motif phosphorylation controls formation and lipid transfer function of inter-organelle contacts. EMBO J. *39*, e104369. https://doi.org/10.15252/embj.2019104369.

129. Stamer, K., Vogel, R., Thies, E., Mandelkow, E., and Mandelkow, E.M. (2002). Tau blocks traffic of organelles, neurofilaments, and APP vesicles in neurons and enhances oxidative stress. J. Cell Biol. *156*, 1051–1063. https://doi.org/10.1083/jcb.200108057.

130. Schikorski, T., Young, S.M., Jr., and Hu, Y. (2007). Horseradish peroxidase cDNA as a marker for electron microscopy in neurons. J. Neurosci. Methods *165*, 210–215. https://doi.org/10.1016/j.jneumeth.2007.06.004.

131. Sannerud, R., Declerck, I., Peric, A., Raemaekers, T., Menendez, G., Zhou, L., Veerle, B., Coen, K., Munck, S., De Strooper, B., et al. (2011). ADP ribosylation factor 6 (ARF6) controls amyloid precursor protein (APP) processing by mediating the endosomal sorting of BACE1. Proc. Natl. Acad. Sci. USA *108*, E559–E568. https://doi.org/10.1073/pnas.1100745108.

132. Nyabi, O., Bentahir, M., Horré, K., Herreman, A., Gottardi-Littell, N., Van Broeckhoven, C., Merchiers, P., Spittaels, K., Annaert, W., and De Strooper, B. (2003). Presenilins mutated at Asp-257 or Asp-385 restore Pen-2 expression and Nicastrin glycosylation but remain catalytically inactive in the absence of wild type Presenilin. J. Biol. Chem. *278*, 43430–43436. https://doi.org/10.1074/jbc.M306957200.

133. Schneider, C.A., Rasband, W.S., and Eliceiri, K.W. (2012). NIH Image to ImageJ: 25 years of image analysis. Nat. Methods *9*, 671–675. https://doi.org/10.1038/nmeth.2089.

134. Kilpatrick, B.S., Eden, E.R., Schapira, A.H., Futter, C.E., and Patel, S. (2013). Direct mobilisation of lysosomal Ca2+ triggers complex Ca2+ signals. J. Cell Sci. *126*, 60–66. https://doi.org/10.1242/jcs.118836.

135. Canton, J., and Grinstein, S. (2015). Measuring lysosomal pH by fluorescence microscopy. Methods Cell Biol. *126*, 85–99. https://doi.org/10.1016/bs.mcb.2014.10.021.

136. Serra-Peinado, C., Sicart, A., Llopis, J., and Egea, G. (2016). Actin Filaments Are Involved in the Coupling of V0-V1 Domains of Vacuolar H+-ATPase at the Golgi Complex. J. Biol. Chem. *291*, 7286–7299. https://doi.org/10.1074/jbc.M115.675272.

137. Lafourcade, C., Sobo, K., Kieffer-Jaquinod, S., Garin, J., and van der Goot, F.G. (2008). Regulation of the V-ATPase along the endocytic pathway occurs through reversible subunit association and membrane localization. PLoS One *3*, e2758. https://doi.org/10.1371/journal.pone.0002758.

138. Bolte, S., and Cordelières, F.P. (2006). A guided tour into subcellular colocalization analysis in light microscopy. J. Microsc. *224*, 213–232. https://doi.org/10.1111/j.1365-2818.2006.01706.x.

139. Sibarita, J.B. (2014). High-density single-particle tracking: quantifying molecule organization and dynamics at the nanoscale. Histochem. Cell Biol. *141*, 587–595. https://doi.org/10.1007/s00418-014-1214-1.

140. Miura, K. (2020). Bleach correction ImageJ plugin for compensating the photobleaching of time-lapse sequences. F1000Res *9*, 1494. https://doi.org/10.12688/f1000research.27171.1.

141. Haase, R., Royer, L.A., Steinbach, P., Schmidt, D., Dibrov, A., Schmidt, U., Weigert, M., Maghelli, N., Tomancak, P., Jug, F., and Myers, E.W. (2020). CLIJ: GPU-accelerated image processing for everyone. Nat. Methods *17*, 5–6. https://doi.org/10.1038/s41592-019-0650-1.

142. Tsai, W.-H. (1985). Moment-preserving thresolding: A new approach. Comput. Vision Graphics Image Process. *29*, 377–393. https://doi.org/10.1016/0734-189X(85)90133-1.

143. Reynolds, E.S. (1963). The use of lead citrate at high pH as an electron-opaque stain in electron microscopy. J. Cell Biol. *17*, 208–212. https://doi.org/10.1083/jcb.17.1.208.

Please cite this article in press as: Bretou et al., Accumulation of APP C-terminal fragments causes endolysosomal dysfunction through the dysregulation of late endosome to lysosome-ER contact sites, Developmental Cell (2024), https://doi.org/10.1016/j.devcel.2024.03.030

STAR★METHODS

KEY RESOURCES TABLE

REAGENT or RESOURCE	SOURCE	IDENTIFIER
Antibodies		
Rabbit polyclonal anti-PSEN2-CTF	Herreman et al.[117]	B24
Rabbit polyclonal anti-APP	Esselens et al.[32]	B63
Mouse monoclonal anti-NCT	Esselens et al.[32]	9C3
Rabbit polyclonal anti-ICAM5	Esselens et al.[32]	B36
Mouse monoclonal anti-CD147	Abcam	Cat#ab666: RRID:AB_305632
Rabbit polyclonal anti-PSEN1-NTF	Abcam	Cat#ab71181; RRID: AB_1603935
Rabbit polyclonal anti-PEN2	Abcam	Cat#18189; RRID: AB_444310
Rabbit polyclonal anti-EEA1	Sigma-Aldrich	Cat#E4156; RRID: AB_609870
Rabbit polyclonal anti-V-ATPase A1	Santa-Cruz	Cat#sc-28801; RRID: AB_2258865
Rabbit polyclonal anti-LC3B	Novus Biological	Cat#NB600-1384; RRID: AB_669581
Rabbit polyclonal anti-caveolin1	BD Bioscience	Cat#610060; RRID: AB_397472
Mouse monoclonal anti-caveolin1	BD Bioscience	Cat#610407; RRID: AB_397789
Goat polyclonal anti-VPS35	Abcam	Cat#ab10099; RRID: AB_296841
Mouse monoclonal anti-beta actin	Sigma-Aldrich	Cat#A5441; RRID: AB_476744
Mouse monoclonal anti-V0d1	Abcam	Cat#ab56441; RRID: AB_940402
Mouse monoclonal anti-V1b2	Santa-Cruz	Cat#sc-166122; RRID: AB_2258897
Mouse monoclonal anti-HSP60	BD transduction	Cat#611562; RRID: AB_399008
Mouse monoclonal anti-PtdIns(3,5)P2	Echelon Biosciences	Cat#Z-P035; RRID: AB_427224
Mouse monoclonal anti-VPS35	Santa-Cruz	Cat#sc-374372; RRID: AB_10988942
Mouse monoclonal anti-Abeta 82E1	Tecan	Cat#JP10323; RRID: AB_1630806
Mouse monoclonal anti-FLAG	Sigma-Aldrich	Cat#F1804; RRID: AB_262044
Rat monoclonal anti-LAMP1	Santa-Cruz	Cat#sc-19992; RRID: AB_2134495
Rabbit monoclonal anti-APP (Y188)	Abcam	Cat#ab32136; RRID: AB_2134495
Goat anti-Mouse IgG (H+L) Highly Cross-Adsorbed Secondary Antibody-Alexa-488	ThermoFisher Scientific	Cat#A-11029; RRID: AB_2534088
Goat anti-Mouse IgG (H+L) Highly Cross-Adsorbed Secondary Antibody-Alexa-568	ThermoFisher Scientific	Cat#A-11031; RRID: AB_144696
Goat anti-Mouse IgG (H+L) Highly Cross-Adsorbed Secondary Antibody-Alexa-647	ThermoFisher Scientific	Cat#A-21236; RRID: AB_2535805
Goat anti-Rabbit IgG (H+L) Highly Cross-Adsorbed Secondary Antibody-Alexa-488	ThermoFisher Scientific	Cat#A-11034; RRID: AB_2576217
Goat anti-Rabbit IgG (H+L) Highly Cross-Adsorbed Secondary Antibody-Alexa-568	ThermoFisher Scientific	Cat#A-11036; RRID: AB_10563566
Goat anti-Rabbit IgG (H+L) Highly Cross-Adsorbed Secondary Antibody-Alexa-647	ThermoFisher Scientific	Cat#A-21245; RRID: AB_141775
Goat anti-Rat IgG (H+L) Cross-Adsorbed Secondary Antibody, Alexa Fluor™ 647	ThermoFisher Scientific	Cat#A-21247; RRID: AB_141778
Donkey anti-mouse IgG (H+L) Highly Cross-Adsorbed Secondary Antibody-Alexa-488	ThermoFisher Scientific	Cat#A-21202; RRID: AB_141607
Donkey anti-goat IgG (H+L) Highly Cross-Adsorbed Secondary Antibody-Alexa-488	ThermoFisher Scientific	Cat#A-11055; RRID: AB_2534102
Donkey anti-mouse IgG (H+L) Highly Cross-Adsorbed Secondary Antibody-Alexa-647	ThermoFisher Scientific	Cat#A-31571; RRID: AB_162542
Donkey anti-goat IgG (H+L) Highly Cross-Adsorbed Secondary Antibody-Alexa-555	ThermoFisher Scientific	Cat#A-21432; RRID: AB_141788
Goat anti-mouse -HRP	BioRad	Cat#1706516; RRID: AB_2921252

(*Continued on next page*)

Please cite this article in press as: Bretou et al., Accumulation of APP C-terminal fragments causes endolysosomal dysfunction through the dysregulation of late endosome to lysosome-ER contact sites, Developmental Cell (2024), https://doi.org/10.1016/j.devcel.2024.03.030

Continued

REAGENT or RESOURCE	SOURCE	IDENTIFIER
Rabbit anti-goat-HRP	Dako	Cat#P044901
Rabbit anti-Rat-HRP	Dako	Cat#P045001
Goat anti-Rabbit-HRP	BioRad	Cat#170-6515; RRID: AB_11125142
Bacterial and virus strains		
Subcloning Efficiency DH5α Competent Cells	ThermoFisher Scientific	Cat#18265017
Chemicals, peptides, and recombinant proteins		
Lysotracker Red DND-99	ThermoFisher Scientific	Cat#L7528
Lysotracker Deep Red	ThermoFisher Scientific	Cat#L12492
Mitotracker Deep Red	ThermoFisher Scientific	Cat#M22426
Cholera Toxin Subunit B Alexa 488	ThermoFisher Scientific	Cat#C34775
Cholera Toxin Subunit B Alexa 647	ThermoFisher Scientific	Cat#C34778
Phalloidin Alexa 488	ThermoFisher Scientific	Cat#A12379
Phalloidin Alexa 568	ThermoFisher Scientific	Cat#A12380
Phalloidin Alexa 647	ThermoFisher Scientific	Cat#A22287
Filipin III Streptomyces filipensis	Sigma-Aldrich	Cat#F4767
DAPT	Tocris	Cat#2634; CAS 208255-80-5
InSolution™ γ-Secretase Inhibitor X	Calbiochem	Cat#565771
β-Secretase Inhibitor IV	Calbiochem	Cat#565788; CAS : 797035-11-1
(2-Hydroxypropyl)-γ-cyclodextrin	Sigma-Aldrich	Cat#H125; CAS : 128446-34-4
ADAM10 inhibitor G1254023X	Sigma-Aldrich	Cat#SML0789; CAS : 260264-93-5
OSW-1 (Orsaponin)	Cayman	Cat #30310; CAS : 145075-81-6
Bafilomycin A1	Bio-Connect	Cat#88899-55-2; CAS : 88899-55-2
Fura2-AM	Thermo Fisher Scientific	Cat#F1221
Thapsigargin	Thermo Fisher Scientific	Cat#T7459
GPN	Abcam	Cat#ab145914
MLSA1	Tocris	Cat#4746
Ionomycin	Sigma-Aldrich	Cat#I0634
monensin	Sigma-Aldrich	Cat#M5273
Nigericin	Thermo Fisher Scientific	Cat# N1495
2-hydroxypropyl-γ-cyclodextrin	Sigma-Aldrich	Cat#H125-5G-I
SidK-AL568	Gift from John L. Rubinstein, SickKids, University of Toronto, Canada, Maxson et al.[36]	N/A
Polybrene	Sigma-Aldrich	cat#H9268
Critical commercial assays		
QuikChange II XL Site-Directed Mutagenesis Kit	Agilent	Cat# 200517
NEBuilder HiFi DNA Assembly Master Mix	New England Biolabs	Cat# E2621S
Experimental models: Cell lines		
MEF PSEN1 and 2 knock out	Escamilla-Ayala et al.[2]	N/A
MEF PSEN1 and 2 knock out, APP knock out	This paper	N/A
MEF PSEN1 and 2 knock out rescued with PSEN1	This paper	N/A
MEF PSEN1 and 2 knock out, APP knock out rescued with APP	This paper	N/A
MEF PSEN1 and 2 knock out, APP knock out rescued with C99	This paper	N/A
MEF PSEN1 and 2 knock out, APP knock out rescued with C83	This paper	N/A
MEF PSEN1 and 2 knock out, APP knock out rescued with mAICD	This paper	N/A
MEF PSEN1 and 2 knock out, APP knock out rescued with mAICD-(AENPTA)	This paper	N/A

(*Continued on next page*)

Please cite this article in press as: Bretou et al., Accumulation of APP C-terminal fragments causes endolysosomal dysfunction through the dysregulation of late endosome to lysosome-ER contact sites, Developmental Cell (2024), https://doi.org/10.1016/j.devcel.2024.03.030

Continued

REAGENT or RESOURCE	SOURCE	IDENTIFIER
HeLa	Tharkeshwar et al.[118]	N/A
HeLa NPC1 knock-out	Tharkeshwar et al.[118]	N/A
HEK293 T	ATCC	Cat#CRL-11268, RRID:CVCL_1926
Experimental models: Organisms/strains		
Mouse: C57BL/6JAX	The Jackson Laboratory	RRID:IMSR_JAX:000664
Mouse: C57BL/6JAX TRPML1 x Gcamp6	This paper	N/A
Mouse: PS1 -/+	De Strooper et al.[119]	N/A
Mouse: C57BL/6 TRPML1-Gcamp6 x PS1-/+	This paper	N/A
Oligonucleotides		
Primer forward C99 to C83: ggcggatgcggatgcattggtgttctttgcag	Integrated DNA Technologies	N/A
Primer reverse C99 to C83: acgcgtacgcgtctagttctgcatctgctcaaag	Integrated DNA Technologies	N/A
Primer forward APP: tctagatctagagccaccatgctgcccggtttggcactg	Integrated DNA Technologies	N/A
Primer reverse APP: acgcgtacgcgtctagttctgcatctgctcaaag	Integrated DNA Technologies	N/A
Primer forward C99: tctagatctagaatgctgcccggtttggcactgc	Integrated DNA Technologies	N/A
Primer reverse C99: acgcgtacgcgtctagttctgcatctgctcaaagaacttgtagg	Integrated DNA Technologies	N/A
gBlock for mCtrl: CCTCCATAGAAGACACCGACTCTAGATGGGCTGCAT CAAGAGCAAGCGCAAGGACAACCTGAACGACGACG GCGTGGACATGAAGACCATGGTGAGCAAGGGCGAG GAGCTGTTCACCGGGGTGGTGCCCATCCTGGTCGA GCTGGACGGCGACGTAAACGGCCACAGGTTCAGC GTGTCCGGCGAGGGCGAGGGCGATGCCACCTACG GCAAGCTGACCCTGAAGTTCCGCTTCCTGGAAGAA CGACCTTGACGCGTGCTCTAGCCCAATTCCGCC	Integrated DNA Technologies	N/A
gBlock for mAICD: CCTCCATAGAAGACACCGACTCTAGATGGGCTGCAT CAAGAGCAAGCGCAAGGACAACCTGAACGACGACG GCGTGGACGGACGCGTAAAGAAGAAACAGTACACA TCCATTCATCATGGTGTGGTGGAGGTTGACGCCGCT GTCACCCCAGAGGAGCGCCACCTGTCCAAGATGCA GCAGAACGGCTACGAAAATCCAACCTACAAGTTCTT TGAGCAGATGCAGAACCGCTTCCTGGAAGAACGAC CTTGACGCGTGCTCTAGCCCAATTCCGCC	Integrated DNA Technologies	N/A
gBlock for mAICD Y682A_Y687A CCTCCATAGAAGACACCGACTCTAGATGGGCTGCATC AAGAGCAAGCGCAAGGACAACCTGAACGACGACGGC GTGGACGGACGCGTAAAGAAGAAACAGTACACATCCA TTCATCATGGTGTGGTGGAGGTTGACGCCGCTGTCAC CCCAGAGGAGCGCCACCTGTCCAAGATGCAGCAGAA CGGCGCCGAAAATCCAACCGCCAAGTTCTTTGAGCAG ATGCAGAACCGCTTCCTGGAAGAACGACCTTGACGC GTGCTCTAGCCCAATTCCGCC	Integrated DNA Technologies	N/A
Recombinant DNA		
pFUGW-FIRE-pHLy	Addgene; Chin et al.[35]	RRID: Addgene_170774; Chin et al.[35]
mcherry-Sec61b	Addgene; Ma and Mayr[120]	RRID: Addgene_121160
pAc-GFPC1-Sec61b	Addgene; Shibata et al.[121]	RRID: Addgene_15108
mCherry-VAPB	Addgene; Zewe et al.[122]	RRID: Addgene_108126
Flag-Stard3-wt	Gift from F. Aply	N/A

(*Continued on next page*)

Continued

REAGENT or RESOURCE	SOURCE	IDENTIFIER
C99-FLAG	Gift from Lawrence Rajendran, King's College London, UK	N/A
C99-GFP	Gift from Lawrence Rajendran, King's College London, UK. Rajendran	N/A
APP-YFP	Gift from Eva-Maria Mandellkow, DZNE, Bonn, Germany.	N/A
HRP-KDEL	Gift from Francesca Giordano, Institute of Integrative Cell Biology, Paris Sud, France.	N/A
pMSCV-PSEN1	Coen et al.[24]	N/A
pCHMWS-mAICD-ires-puromycin	This paper	N/A
pCHMWS-mCtrl-ires-puromycin	This paper	N/A
pCHMWS-mAICD-Y682A-Y687-ires-puromycin	This paper	N/A
pCHMWS-C99-ires-puromycin	This paper	N/A
pCHMWS-C83-ires-puromycin	This paper	N/A
pCHMWS-APP	This paper	N/A
Software and algorithms		
ImageJ	Schindelin et al.[123]	https://imagej.nih.gov/ij/; RRID: SCR_002285
GraphPad Prism 9	GraphPad	https://www.graphpad.com/; RRID: SCR_000306
Adobe Illustrator CS6	Adobe	https://www.adobe.com/products/illustrator.html; RRID: SCR_010279
Aida Image Analyzer software	Raytest	https://www.elysia-raytest.com; RRID: SCR_014440
Metamorph PALM tracer software	J.B. Sibarita	https://www.iins.u-bordeaux.fr/team-sibarita-PALMTracer
BioRender	BioRender	https://www.biorender.com/; RRID: SCR_018361

RESOURCE AVAILABILITY

Lead contact

Further information and requests for resources and reagents should be directed to and will be fulfilled by the lead contact, Wim Annaert (wim.annaert@kuleuven.be).

Materials availability

Materials generated in this study are available upon request.

Data and code availability

All data reported in this study will be shared by the lead contact upon request.

This paper does not report original codes.

Any additional information required to reanalyze the data reported in this work paper is available from the lead contact upon request.

EXPERIMENTAL MODEL AND STUDY PARTICIPANT DETAILS

Animal

Mice

TRPML1-Gcamp6 mouse generation. TRPML1-Gcamp6 mice were produced by Ingenious targeting laboratory, and were obtained using the *CRISPR-Assisted Reporter Knock-in Targeting Vector Construction* strategy. Briefly, a targeting vector bearing homology arms, Gcamp6 and a selection cassette (Neo) was designed, using conventional cloning method. Colony PCR was used to amplify both 5' and 3' homology arms with about 820 bp and 1.3 kb in length, respectively, from a positively identified C57BL/6 BAC clone (RP23-298P17); the GCAMP6s was fused at the ATG start site in exon 1 of the TRPML1 gene and a Neo cassette was inserted

downstream of the potential promoter sequence in intron 1-2. This combination was cloned in to the iTL cloning vector (~2.45 kb) derived from pSP72 (Promega). The validated targeting vector was electroporated in embryonic stem (ES) cells, and resulting clones were screened by PCR and Southern Blotting. Targeted clones were microinjected into Balb/c blastocysts, and resulting chimeras were mated to C57BL/6 WT mice to generate Germline Neo deleted mice, leaving only the Gcamp6 reporter inserted. PSEN1WT or KO-TRPML1 Gcamp6 mice were obtained by crossing TRPML1-Gamp6 KI/KI with WT and PSEN1 KO mice.

All mice experiments were conducted according to protocols approved by the local Ethical Committee of Laboratory Animals of the KU Leuven (government license LA1210579, ECD project number P173/2022) following local and EU guidelines.

Cell culture and primary hippocampal neuron culture

Mouse embryonic fibroblasts (MEFs) were maintained in DMEM-F12 (Invitrogen) containing 10% FCS and maintained in a humidified chamber with 5 % CO2 at 37°C.

NPC1KO Human cervical cancer cells (Hela) were characterized and cultured as described in [118].

Primary hippocampal neuron cultures were obtained as previously described.[24,32] Briefly, hippocampal neurons were derived from embryonic day 17 embryos from heterozygous crosses and were co-cultured with a glial feeder layer to allow proper neuronal differentiation and polarization. After dissociation, cells from hippocampi of individual embryos were plated on poly-l-lysine–coated coverslips in minimal essential medium (MEM) supplemented with 10% (vol/vol) horse serum. Twenty hours after plating, culture medium was replaced by serum-free neurobasal medium supplemented with B27 (Gibco). 5-Fluoro-2′-deoxyuridine (F0503, Sigma, 10 μM final) was added at DIV (days in vitro) 4, to prevent glial proliferation. Hippocampal neurons were maintained at 37°C and 5% CO_2 for the indicated time.

METHOD DETAILS

Antibodies and reagents

Rabbit polyclonal antibodies (pAb) to PSEN2-CTF (B24 1/2000 for WB), APP (B63.1, 1/5000 for WB), and monoclonal antibody (mAb) to NCT (9C3, 1/7000 for western blotting (WB)) were used as described.[32,124–127] The following antibodies were commercially obtained: rabbit pAb anti-PSEN1 NTF (ab71181, abcam, 1/3000 for WB), anti-PSEN1 CTF (ab24748, abcam, 1/1000 for WB), anti-PEN2 (ab18189, abcam, 1/1000 for WB), anti-EEA1 (E4156, Sigma, 1/300 in IF, 1/250 for WB), anti-V-ATPase A1 (v0a1, H-140, sc-28801, Santa Cruz Biotechnology 1/1000 for WB), anti-LC3B (NB600-1384H, Novus Biological, 1/2000 for WB), anti-caveolin1 (610060 and 610407, BD Biosciences, 1/200 in IF); goat pAB anti-VPS35 (ab10099, abcam, 1/250 in IF); mouse mAb anti-β actin (AC15, A5441, Sigma Aldrich, 1/10000 for WB), anti-V0d1 (ab56441, abcam, 1/1000 for WB), anti-V1b2 (sc-166122, Santa Cruz Biotechnology, 1/1000 for WB), anti-HSP60 (611562, BD transduction 1/200 in IF), anti-PtdIns (3,5)P2 (Z-P035-2-EC, Echelon, mobitec, 1/200 in IF), anti-VPS35 (sc-374372, Santa Cruz Biotechnology, 1/500 for WB), anti-human Aβ 82E1 (JP10323, Tecan, 1/100 in IF), anti-Flag (F1804, Sigma, 1/500 in IF); rat mAb anti-LAMP1 (sc-19992, Santa Cruz, 1:300 in IF, 1/1000 for WB); rabbit mAb anti-APP (Y188, ab32136, abcam, 1/500 in IF). Peroxidase-conjugated secondary antibodies were purchased from Biorad (1/10000 for WB). Alexa-conjugated fluorescent secondary antibodies (Goat or Donkey, Alexa 488, 555 and 647) were from Life Technologies (1/1000 in IF).

Lysotracker (Red DND-99 L7528, Deep Red L12492, used at 1/20000), Mitotracker (Deep Red, M22426, used at 500 nM), CtxB conjugated with Alexa dyes (-488 C34775, -647 C34778) and phalloidin conjugated with Alexa fluor (-488 A12379; -568 A12380 and -647 A22287) were purchased from ThermoFisher Scientific; Filipin III Streptomyces filipensis (F4767, 200μg.ml^{-1}) from Sigma.

Drug treatments

Cells were treated with the following drugs, for 4 days, unless otherwise stated: DAPT (2634/10, Tocris), 1 μM final; Inhibitor X (565771-250 ug, Calbiochem/Merck), 1 μM final; β-Secretase Inhibitor IV (565788, Calbiochem/Merck), 2 μM final, (2-Hydroxypropyl)-γ-cyclodextrin (H125-5G-I, Sigma Aldrich), 1 mM final; ADAM10 inhibitor G1254023X (SML0789, Sigma Aldrich), 3 μM final. For OSW-1 (30310-1, Sanbio/Cayman Chemical), cells were treated overnight with 10 nM. Bafilomycin A1 (88899-55-2, Bio-connect) was applied at a final concentration of 200 nM for 2 h (see Lysosomal pH measurement with FIRE-pHLy) or at 500 nM for 20 or 40 min (see Figure S2B). Diluent treatment alone (in most cases DMSO, water case of cyclodextrin) was used as vehicle control.

Plasmids and Cell transfection

Cells were transfected using Fugene HD (E2311, Promega), according to the manufacturer's protocol (ratio 4:1 for Fugene HD reagent: DNA was applied). The following plasmids were used: pFUGW-FIRE-pHLy (Addgene plasmid #170774)[35], mCherry-Sec61B (Addgene plasmid # 121160)[120]; pAc-GFPC1-Sec61beta (Addgene plasmid # 15108)[121]; mCherry-VAPB (Addgene plasmid # 108126)[122]; Flag-Stard3-WT (gift from F. Alpy)[128]; C99-GFP (gift from L. Rajendran); APP-YFP (gift from E. M. Mandelkow)[129]; HRP-KDEL (gift from F. Giordano).[130] For all experiments, assays were carried out 24 h after transfection.

For the stable cell line generation, the following plasmids were used: pCHMWS-hAPP695, which was obtained by generating the cDNA APP695wt via PCR, using the plasmid pCDNA-APP695[131] as the template together with the forward and reverse primers specified in the KRT table. The resulting fragment and the pCHMWS plasmid underwent a double digestion using XbaI and MluI followed by ligation. pCHMWS-c99-ires hygromycin was obtained by generating the cDNA C99 via PCR, using the plasmid pCDNA-APP695[131] as the template together with the forward and reverse primers specified in the KRT table. The resulting fragment and the pCHMWS plasmid underwent a double digestion using XbaI and MluI followed by ligation. pCHMWS-C83 was obtained using

Please cite this article in press as: Bretou et al., Accumulation of APP C-terminal fragments causes endolysosomal dysfunction through the dysregulation of late endosome to lysosome-ER contact sites, Developmental Cell (2024), https://doi.org/10.1016/j.devcel.2024.03.030

the QuikChange II XL Site-Directed Mutagenesis Kit (cat# 200517, Agilent) with the forward and reverse primers indicated in the KRT table, according to the manufacturer's instructions. pCHMWS-mCtrl, pCHMWS-mAICD, pCHMWS-mAICDYY were cloned between XbaI and MluI restriction sites. gBlocks fragment corresponding to the sequence of mCtrl, mAICD, and mAICD_YY were obtained from IDT (see key resources table). pCHMWS vector was linearised using XbaI and MluI and assembled with the gBlocks using DNA assembly according to the manufacturer (NEBuilder HiFi DNA Assembly Master Mix, cat# E2621S). All constructs were verified by sequencing.

Generation of stable cell lines

KO cell lines

PSEN1 and 2 KO cell lines (PSENdKO) cell lines were established as described.[2] Briefly, the web-based CRISPR design tool was used to select the sequence to be targeted in mouse PSEN1 and PSEN2 (i.e. 5-CAACGTTATCAAGTACCTCCCCGAA-3' and 5'-CAACGTCCTGGGCGACCGTCGGGCC-3', respectively). Oligo pairs encoding guide sequences (obtained from Integrated DNA Technologies, IDT) were annealed and ligated into the pX330 plasmid (Addgene) according to the Zhang's laboratory protocol (https://www.addgene.org/crispr/zhang/). MEF cells were then transfected with the pX330-PSEN1 and PX330-PSEN2, using Fugene HD (Promega), in accordance with the manufacturer protocol. Selection of PSENdKO clones was achieved through serial dilution and confirmed by WB analysis. Deficiency for APP in WT and different PSENdKO clones was achieved through electroporation of RNP complexes. Single guide RNAs (sgRNAs) were designed to either target exon 2 (5'-GTACCCACTGATGGCAACGC CGG-3') or exon 3 (5'-ACGGTAAGGAATCACGATGT GGG-3'). The Neon Transfection System (ThermoFisher Scientific, one pulse, 1650 V, 20 ms) was used to electroporate 150 000 cells with 10 pmol of Cas 9 (IDT) and 20 pmol of single guide RNA (IDT). As above, cells were amplified and selection of independent APPKO clones was performed with serial dilutions and WB analysis. Selected clones were sequenced using Sanger sequencing.

Rescue cell lines

Cell lines were stably rescued using retro- or lentiviral particles. For virus generation (either retro- or lentivirus), HEK293T cells were transfected using FuGENE6 (Promega) according to the manufacturer's protocol. For retrovirus packaging, pMSCV expressing the gene of interest was co-transfected with the helper plasmid pIk (Ecopac). Of note, cDNA of human WT PSEN1 was already cloned in the retroviral vector PMSCV*-puromycin (Takara bio Inc).[24,132] For lentiviral production, particles were produced by co-transfecting the HEK293T cells with the plasmid of interest, pCMV-ΔR8.74 (for packaging) and pMD2.G (VSV-G, for envelope). In all cases, medium containing the viral particles was collected after 24 h and filtered (0.45 μm filters). For transduction, viral particles were diluted in polybrene containing medium (8 ng/μl, Sigma Aldrich). Medium was refreshed 24 h after the transduction and selection of transduced cells was achieved through antibiotic selection (puromycin, 3 μg/ml, Sigma Aldrich). Stable pools were validated by WB analysis.

Western blotting

Whole cell extracts were prepared from 80% confluent cell cultures and protein concentration determined using the Bio-Rad DC protein assay (Bio-Rad). Denatured extracts were run on 4-12 % Bis-Tris Bolt or NuPAGE precast gels in MES/MOPS running buffer (Invitrogen), followed by transfer on nitrocellulose membranes (Life Technologies). Of note, for APP-CTFs characterization, samples were run on 16% tricine gels in the appropriate running buffer (LC1675, Life Technologies). Membranes were blocked with 5% non-fat milk (1 h, RT), incubated with primary antibodies (overnight, 4°C), rinsed and incubated with HRP-conjugated secondary antibodies (1 h, RT). Immuno-detection was carried out using Western Lightning-Plus ECL reagent (NEL105001EA, PerkinElmer). Immunoreactive protein bands were digitally imaged on a Fuji MiniLAS 3000 imager (Fuji, Düsseldorf, Germany) and analyzed using the Aida Image Analyzer software (Raytest, Germany) or Image J.[123,133]

EndoH-EndoF assay

The EndoH-EndoF assay was carried out as described.[24] Briefly, cell extracts were treated with either EndoH or EndoF (P0702L and P0705L, Bioke, New England Biolabs), according to the manufacturer's protocol. Cell extracts (40 μg) were loaded on 4-20% Tris Glycine gels (Novex, ThermoFisher Scientific) and transferred on PVDF membranes for WB analysis.

Calcium dynamics

Cytosolic response

Ca^{2+} responses were measured as previously described.[24] Briefly, cells (0.005 to 0.01* 10^6) were seeded two to three days prior to the experiment on glass coverslips (631-0153, VWR). On the day of recording, cells were rinsed three times in Ringer solution (155 mM NaCl, 5 mM KCl, 2 mM $MgCl_2$, 2 mM $CaCl_2$, 10 mM Glucose, 10 mM HEPES, 2 mM $NaH_2PO4.2H20$; pH 7.3), and loaded with 1 μM Fura2-AM (F1221, ThermoFisher Scientific) for 30 min (RT). Cells were rinsed three times and left to equilibrate for at least 15-20 min (RT). All acquisitions were carried out in Ringer Ca^{2+} free solution (same as above, albeit the 2 mM $CaCl_2$ was replaced by 2 mM EGTA). During experiments, cells were challenged with different drugs, including Thapsigargin (T7459, ThermoFisher Scientific, 1 μM final), GPN (ab145914, Abcam, 100 μM final for MEFs, 500 μM for neurons), MLSA1 (Cat. No. 4746, Tocris, 20 μM final) or Ionomycin (I0634, Sigma Aldrich, 1 μM final). Images were acquired every 5 sec for 8-10 min, using an Olympus IX81 equipped with an APO/340 40x oil objective (1.35 NA), operated by CellR Software (Olympus). Recordings were done using 340 and 380nm excitation, and 530 nm emission filters. Image processing was performed using Image J. Briefly, cells were segmented manually and fluorescence intensities were measured over time. Fura-2 signals were corrected to obtain ΔF/F0 (F0 being the initial signal recorded). For each cell, the area under the curve, corresponding to the aforementioned stimulation, was measured using GraphPad Prism.

TRPML1-Gcamp6 expressing primary neurons

On the day of isolation, neurons were seeded at 1.5*10^5 cells on 3 cm poly-L-Lysine glass coverslips (41001130, Circular 1001/30, Hecht-Assistent, Germany), and were co-cultured with a glial feeder layer (see hippocampal neuron culture). Recordings were carried out from DIV 14 onwards. TRMPL1-Gcamp6 fluorescence was monitored at an excitation wavelength of 470 nm on a Zeiss Axio Observer D1 equipped with a Zeiss 40x/1.30 Oil objective (420460-9900-000), Andor Neo 5.5 camera, Lambda DG-4 Plus light source and EGFP filter set (Chroma, 49002)) and images were acquired every 3 sec (300 ms exposure time), for 20 min. Neurons were bathed in Ringer solution, and lysosomal Ca^{2+} release elicited by local application of various drugs (20μM MLSA1 for 2 min, 500 μM GPN for 1 min) was measured in absence of extracellular Ca^{2+} (free Ca^{2+} Ringer buffer). For local application, a custom-made multi-barrel was used in combination with a fast-stepper piezo (Sutter SF-77C) and a gravity-based perfusion system (Warner, VC-6). Local application was precisely timed using a HEKA trigger interface (TIB14) in combination with dedicated software (HEKA Patchmaster). When drugs were applied sequentially, resting phases were added (3 min after MLSA1 stimulation, 7 min after GPN application). Baseline fluorescence was determined for 30 sec prior to application. Continuous flow of regular Ringer solution from a control barrel under baseline and resting periods ensured proper wash-out of applied drugs from the recording area. Experiments were done at room temperature. Analysis was carried out as described above.x

Lysosomes-ER refilling assay

The same approach as in[51] was used. Briefly, cells loaded with Fura2-AM were repeatedly challenged with GPN (100 μM-for 5 min). These stimulations were done in Ca^{2+} free Ringer buffer, to ensure that the monitored Ca^{2+} response could be attributed to intracellular lysosomal Ca^{2+}.[31,51] In between stimulation, Ca^{2+} containing Ringer was perfused (for 15 min) to allow the resealing and the refilling of the ruptured lysosomes.[51,134] Analysis was performed as above, and the ratio of the area under the curve measured after the second over the one after the first GPN stimulation were computed (ratio GPN2/GPN1).

Lysosomal pH measurement

Fluorescein dextran

Lysosomal pH measurements were performed as in.[135] Briefly, one day prior to the experiment, cells plated on coverslips (631-0153, VWR) were pulsed for 2 h with 0.2 mg/ml of Fluorescein-dextran (10 000 MW; Sigma-Aldrich), extensively rinsed and incubated overnight to chase the fluorescein-dextran to lysosomes. All acquisitions were carried out at 37°C in HBSS medium supplement with Ca^{2+} and Mg^{2+} but without phenol red, on an inverted microscope (IX81; Olympus) equipped with an 100×/1.35 NA oil objective lens and FvII camera (Olympus soft imaging solution) and operated by Cell^R software (Olympus). Recordings were done with 440 and 490 nm excitation and 520 nm emission filters. A calibration curve was obtained by perfusing cells with a solution of known pH (ranging from 4.0 to 7.0). Cells were treated with ionophores (10 μM nigericin (N1495, ThermoFisher Scientific) and 10 μM monensin (M5273, Sigma Aldrich)). Analysis was carried out using Image J to measure lysosomal pH, the 490 nm signal (background corrected) was normalized by the 440 nm signal (also background subtracted). All values were averaged to provide the mean lysosomal pH in a given cell.

Fire-pHLy

Cells, seeded at a density of 1.5*10^5 cells per well (6 well plates (M8562-100EA, Greiner Cellstar, Sigma-Aldrich) with 13 mm glass coverslips (631-1578, VWR)), were transfected the next day with 2 μg of pFUGW-FIRE-pHLy for 6 h prior to recording.[35] Cells were incubated in OptiMEM for the duration of the transfection. Cells were fixed in 4% paraformaldehyde (PFA) /4% sucrose in PBS free of Ca^{2+} and Mg^{2+} ($PBS^{-/-}$) (20 min), and mounted in mowiol. Acquisition was carried out using Zeiss LSM 880 Airyscan with a 40X objective, and 488 nm and 543 nm lasers were used for to acquire mTFP1 and mCherry signals, respectively. Images were analysed using Image J. After background subtraction and smoothening, a mask was created for the lysosomes (using the mCherry signals) and then applied to the corresponding mTFP1 source image. Mean fluorescence intensities of mCherry and mTFP1 channels were compiled, and the ratios were calculated. Bafilomycin treatment (200 nM for 2 h) was performed to confirm the pH-sensitivity of mTFP1.

To localize and quantify ***active V-ATPases proton pumps***, the recombinant Alexa Fluor 568-conjugated SidK (SidK-AL568, gift from M. Maxson) was used.[36] As for immunostaining (see below) cells were fixed with PFA (20 min), and then blocked, permeabilized (30 min with 5% BSA in PBS + 0.1% TritonX-100) and stained with SidK-AL568 (1/200, in the aforementioned buffer). After 30 min, immunolabeling with anti-LAMP1 (for 2 h, 1/200 in blocking buffer (see the immunofluorescence section below) with 5% of goat serum) was performed using Alexa 647-conjugated secondary anti-rat antibodies (1/1000 in blocking buffer, 1 h, RT) for detection. Cells incubated in HBSS (ThermoFisher/Invitrogen) were imaged directly on a Zeiss LSM 880 Airyscan and images analyzed using ImageJ.

Isolation of Late Endosomes/Lysosomes using Super Paramagnetic Iron Oxide Nanoparticles

LE/LYS were isolated according to[118] with some modifications. Confluent cells were incubated with DMSA-coated SPIONs suspended in culture medium (0.2 mg/ml) for 30 min at 37°C. Excess of DMSA-coated SPIONs was washed using PBS and cells were re-incubated overnight in a humidified chamber with 5 % CO_2 at 37 C. Acidic washes (0.15 M glycine, pH 3) were performed to remove SPIONs at the cell surface. After rinsing with PBS, cells were scraped, centrifuged (180 x g, 10 min) and pellets were re-suspended in homogenization buffer (HB; 250 mM sucrose, 5 mM Tris and 1 mM EGTA pH 7.4 supplemented with PI). After cell cracking (12 passages, clearance 10 μm) the total homogenate was centrifuged (800 x g, 10 min) and the post nuclear supernatant (PNS) loaded on a LS column (pre-equilibrated with HB) placed in a strong magnetic field (SuperMACSII, Miltenyi). Cell debris and organelles devoid of DMSA-SPIONs were removed by extensive washes with cold HB after which the magnetic field was removed to elute the bound fraction containing LE/Lys. The eluate was centrifuged (126000 x g, 1 h) and the resulting pellet re-suspended in

200 μl HB. To evaluate the presence of V-ATPase complexes in the purified fractions, the ratio of the V0/V1 domains was evaluated by WB.[136,137]

Suspension-adhesion assay

Suspension-adhesion assays were performed as decribed previously.[39] Briefly, adherent cells were incubated on ice (15 min) with 10 μg/ml CTxB-Alexa488 in $PBS^{-/-}$. Cells were detached with trypsin, washed and held in suspension with 1 % methylcellulose before re-plating on 20 μg/ml fibronectin-coated coverslips. At defined time-points, internalization and endocytic transport/recycling of CTxB-Alexa488 was analysed by immuno-cytochemistry. For the analysis, the number of cells displaying repolarized markers (caveolin1) to the total cells was quantified per field of view.

Mitochondrial metabolism

The oxygen Consumption rate (OCR) of mitochondria was measured with a Seahorse XFe24 Analyzer (Seahorse Biosciences, Billerica, MA) according to the manufacturer's instructions, with minor modifications. Cells were sequentially treated with 1 μM oligomycin, 1 μM FCCP, 0.5 μM rotenone/antimycin A. Data were normalized to protein cell counts and next to the mean of WT control samples. Analysis was performed using the online Seahorse Analytics software.

Confocal microscopy

Immunofluorescence

Cells were fixed in 4% PFA/4% sucrose in Ca^{2+} and Mg^{2+} free PBS ($PBS^{-/-}$, 20 min, RT), permeabilized (0.1% triton X-100 in $PBS^{-/-}$; 10 min, RT), and blocked (2% BSA, 2% FBS, 1% gelatin, and depending on the experiment, 2% of goat or donkey serum (Bioké or Sigma), 1h RT). Primary antibodies diluted in the same blocking buffer were incubated overnight at 4°C, and following PBS washing steps, further incubated with (goat- or donkey-) secondary antibodies conjugated with Alexa fluor dyes (Alexa 488, 568, or 647; ThermoFisher Scientific) diluted in blocking buffer (1h, RT). Coverslips were mounted with Mowiol (Sigma). When cholesterol labelling was performed, fixed cells were treated with 200 μg/ml filipin (F4767, Sigma) for 2 h at RT, prior to permeabilization.

Acquisition

Z stack images (spacing 2 μm), or a median plan were acquired on a Nikon 1AR connected to an inverse Nikon Ti-2000 equipped with an oil-immersion plan APO 60x objective lenses with 1.40 NA. Data were collected using Nikon Imaging Software. For representation, and where needed, images were displayed in false color.

Image analysis

Image analysis was done using Image J software.[123,133] To measure the area of the organelle of interest, segmentation was applied using automatic thresholding. The following masks were used: Mean (EEA1), Ostu (LAMP1), Intermodes (VPS35). Overlap of signals of interests were quantified with Manders' co-localisation index (Plugin Jacob, [138]). When indicated, co-localization data were normalized to the reference group for multiple comparisons.

Airyscan Imaging

Fixed cells

Images of fixed transfected cells (with LAMP1-mCherry and GFP-Sec61b or VAPB-mCherry and Stard3-HA) were acquired using an inverted Zeiss LSM 880 microscope with Airyscan detector in super-resolution mode. The system was equipped with a 63x 1.4 NA Plan-Apochromat objective lens and operated using Zen Black (version 2.3, Carl Zeiss Microscopy GmbH). The excitation lasers Argon 488, 514, He-Ne 543, 594 and 633 were used with the filter set combinations BP 420 – 480 + BP 495–550, BP 420 – 480 + BP 495– 620, BP 420 – 480 + LP 605, BP 465–505 + LP 525, BP 495–550 + LP 570, and BP 570 – 620 + LP 645. Cells with similar levels of transfection were selected. All Airyscan-acquired images were processed using the default values. Obtained images were further processed using the plot profile function of Image J.

Live-imaging of hypotonically treated cells

Transfected cells (with APP-YFP or C99-GFP and mCherry-Sec61b, or treated with mitotracker Deep Red) were treated with hypotonic media (5% DMEM in water, pH∼7, pre-equilibrated at 37°C and 5% CO2) for 10 min at 37°C to allow the formation of the large intracellular vesicles (LICVs).[55] Images were acquired within 15 min using the fast Airyscan mode of a Zeiss LSM880 microscope, equipped with the same objective, lasers and filters as above. Acquired and processed images were analysed using the Image J plot profile feature (*vide supra*).

Live-imaging

Lysosome-mitochondria interactions. Cells were seeded at a density of $0.06*10^6$ on 15 mm glass coverslips (631-1579, VWR). After 2 days, cells were first stained with Deep Red Mitotracker (500nM, in complete medium, for 10 min at 37°C), and next with Lysotracker red (50nM, in HBSS without any extra incubation time). Living cells were directly recorded using a Zeiss LSM 880 Airyscan. Tracking was done using Metamorph PALMtracer software and data analysis was done on Fiji using an ImageJ custom macro.

Structured Illumination microscopy (SIM)

Live cell imaging of cells transiently transfected with mCherry-LAMP1 and GFP-Sec61b were imaged with a two-camera lattice SIM Elyra7 microscope (Carl Zeiss, Jena, Germany) equipped with a Plan Apo 63x 1.4 NA objective lens. Dual colour frames were acquired every 250 ms for about 2 min. SIM reconstruction was done with ZEN black software (Carl Zeiss, Jena, Germany).

For diffusion analysis of lysosomes, ROIs of the same size were made for the whole stack of the mCherry channel. Tracking was done using Metamorph PALMtracer software with Auto thresholding and circularity feature (https://www.iins.u-bordeaux.fr/team-sibarita-PALMTracer). Only tracks with more than 8 points where considered and MSD was calculated by linear fitting of the first four points. MSD of individual tracks were averaged per cell. For type of motility analysis, the alpha was calculated by the power of the MSD. Immobile tracks were defined as those with a diffusion coefficient below the resolution limit of the microscope limit and calculated by the average of MSD (0) of the control cells, rendering a limit of 0.0035um2/s. From the mobile tracks the alpha was classified as follows: <0.1=confined, 0.1 to 0.9=abnormal, 0.9 to 1.1= Brownian, and >1.1 =directed.[139] The D Log_{10} was calculated to analyse different populations.

Colocalization analysis

Analysis was done on Fiji[123] using an ImageJ custom macro. For the mCherry and GFPchannels, a bleach correction using exponential fit[140] was first performed and next normalized using the CLIJX plugin (CLIJx_normalize from 0 to 1).[141] A moment automatic threshold[142] was thereafter performed to create a binary mask. Objects smaller than 20 pixels were excluded and the area of the lysosome and ER was measured for each time point. A Boolean AND operation using the Image Calculator in Fiji was used to create the overlapping image mask between lysosomes and the ER and the overlapping area measured for each time point. In addition, the mean through all the timepoints of the lysosome, ER and overlapping areas were computed.

Transmission Electron microscopy (TEM)

In brief, cells grown in 35 mm culture dishes till 90-95% confluency were fixed in 2.5% glutaraldehyde (Agar Scientific) (overnight, 4°C) and rinsed with 0.1 M sodium cacodylate buffer (pH 7.2) to remove glutaraldehyde.[118] Fixed cells were scraped in washing buffer, centrifuged (200 x g, RT), and the pellet resuspended in 1.5% agarose. After one more centrifugation (400 x g, RT), they were left on ice to solidify (30 min). Samples were post-fixed in 1% osmium tetroxide and 1.5% ferrocyanide (2h), rinsed with dH_2O and dehydrated in a graded ethanol series (from 30-100%). Samples were *en bloc* stained with 4% uranyl acetate in the 70% ethanol step (30 min, 4°C). Following dehydration, samples were infiltrated with epoxy resin/propylene oxide mixtures (50% and 66%). The next day, cell pellets were embedded with 100% epoxy resin in inverted BEEM-capsules (2 days, 60 °C). Ultrathin sections of 70 nm were cut using an ultratome (LEICA REICHERT Ultracut S) and post-stained with 4% uranyl acetate in water (10 min) and Reynolds' lead citrate[143] (5 min). Micrographs were taken on a JEOL JEM 1400 electron microscope equipped with an Olympus Quemesa 11 Mpxl camera at 80 KV.

KDEL-HRP TEM

Cells transiently transfected with KDEL-HRP were fixed in 1.3% glutaraldehyde (Agar Scientific) in 0.1 M sodium cacodylate buffer (pH 7.2; 1 h, RT). After washing in 0.1 M cacodylate buffer to remove glutaraldehyde, cells were incubated in 0.1M ammoniumphosphate (pH 7.4; 1 0min, RT). 3′ 3-Diaminobenzidine tetrahydrochloride (DAB) was dissolved in 0.1 M ammoniumphosphate (0,5 mg/ml), filtered (0,2 μm) to remove any undissolved precipitate and used to wash the cells (10 min, RT). This ammoniumphosphate/DAB mixture was next replaced with ammoniumphosphate/DAB mixture including 0.005% H_2O_2 to generate an insoluble reaction product (15 min, RT). Samples were post-fixed with 1% osmium tetroxide and 1.5% ferrocyanide (1 h) and extensively washed with 0.1 M sodium cacodylate buffer and ddH_2O before being *en bloc* stained with 0.5% uranyl acetate in ddH_2O (overnight, 4°C). Samples were dehydrated in a graded ethanol series (from 30-100%) and further infiltrated in epoxy resin/ethanol mixtures (50% and 66%). As for classical TEM, samples were embedded in epoxy resin (2 days, 60°C); ultrathin sections of 70 nm were cut on an ultratome (LEICA REICHERT Ultracut S) and post-stained with 4% uranyl acetate (10 min) and Reynolds lead citrate (5 min). Using RADIUS 2.0 (Build 14402, EMSIS), the distance between KDEL-HRP positive ER compartments and LE/Lys was measured to identify ER-LE/Lys MCSs, followed by systematic analysis of their length.

QUANTIFICATION AND STATISTICAL ANALYSIS

Statistics and reproducibility

Experiments shown in figures mostly correspond to pooled experiments (n=number of cells analysed, N=number of experiments). Whenever possible, n-values were directly indicated in the graphs, otherwise stated in the corresponding legend. All graphs and statistical analyses were performed using GraphPad Prism (versions 7 or higher), and exact p-values are indicated in the figures. Data are represented as (i) boxes and whiskers; where bars include 90% of the points, the line represents the median, and the box contains 750% of the data or as (ii) mean ± SEM. Comparisons between any two groups were done using the non-parametric Mann-Whitney statistical test; comparison between multiple groups were made using Multiple Anova Kruskal-Wallis with Dunn's post-test, unless otherwise stated.